


Winter 2016

# Kinetic energy harvesting mechanism for vortex drop structures

Mungtra Chusilp

Follow this and additional works at: <https://digitalcommons.latech.edu/dissertations>

 Part of the [Civil Engineering Commons](#), and the [Mechanical Engineering Commons](#)

---

**KINETIC ENERGY HARVESTING MECHANISM  
FOR VORTEX DROP STRUCTURES**

by

**Mungtra Chusilp, B.S., M.S.**

**A Dissertation Presented in Partial Fulfillment  
of the Requirements for the Degree  
Doctor of Philosophy**

**COLLEGE OF ENGINEERING AND SCIENCE  
LOUISIANA TECH UNIVERSITY**

**March 2016**

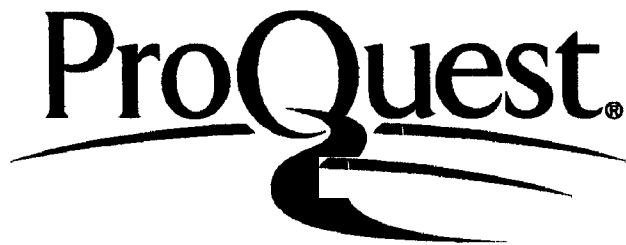
ProQuest Number: 10301425

All rights reserved

**INFORMATION TO ALL USERS**

The quality of this reproduction is dependent upon the quality of the copy submitted.

In the unlikely event that the author did not send a complete manuscript and there are missing pages, these will be noted. Also, if material had to be removed, a note will indicate the deletion.



ProQuest 10301425

Published by ProQuest LLC(2017). Copyright of the Dissertation is held by the Author.

All rights reserved.

This work is protected against unauthorized copying under Title 17, United States Code.  
Microform Edition © ProQuest LLC.

ProQuest LLC  
789 East Eisenhower Parkway  
P.O. Box 1346  
Ann Arbor, MI 48106-1346

LOUISIANA TECH UNIVERSITY

THE GRADUATE SCHOOL

OCTOBER 8, 2015

Date

We hereby recommend that the dissertation prepared under our supervision by

Mungtra Chusilp

entitled Kinetic Energy Harvesting Mechanism for Vortex Drop Structures

be accepted in partial fulfillment of the requirements for the Degree of

Doctor of Philosophy in Engineering

[Signature]

Supervisor of Dissertation Research

[Signature]

Head of Department

Civil Engineering

Department

Recommendation concurred in:

[Signature]  
[Signature]

[Signature]  
[Signature]

Misham Hegab  
Dean of the College

Advisory Committee

Approved:

[Signature]  
Director of Graduate Studies

App: [Signature]  
Dean of the Graduate School  
Dean of the Graduate School

Misham Hegab/SD  
Dean of the College

## **ABSTRACT**

Energy recovery from wastewater is gaining significance as utilities work toward achieving energy neutrality and sustainability in their wastewater collection and treatment systems. In this dissertation, kinetic energy harvesting mechanism for vortex drop structures found within the municipal waste and storm water conveyance systems is presented. There are thousands of sewer drop structures installed across the U.S. carrying billions of gallons of sewage each year. A custom micro water turbine is developed in this research which could be retrofitted within the existing drop shafts to harvest the excessive kinetic energy available. This dissertation presents the conceptual design and analysis of the micro turbine's performance through analytical, numerical and experimental methods. Various measured performance characteristics of a custom built turbine retrofitted within a full scale drop structure installed in a laboratory setting is presented.

## APPROVAL FOR SCHOLARLY DISSEMINATION

The author grants to the Prescott Memorial Library of Louisiana Tech University the right to reproduce, by appropriate methods, upon request, any or all portions of this Dissertation. It is understood that "proper request" consists of the agreement, on the part of the requesting party, that said reproduction is for his personal use and that subsequent reproduction will not occur without written approval of the author of this Dissertation. Further, any portions of the Dissertation used in books, papers, and other works must be appropriately referenced to this Dissertation.

Finally, the author of this Dissertation reserves the right to publish freely, in the literature, at any time, any or all portions of this Dissertation.

Author MUSTRAL CHESIDIP

Date 12/03/2015

## TABLE OF CONTENTS

ABSTRACT.....	iii
LIST OF FIGURES.....	viii
LIST OF TABLES.....	xii
ACKNOWLEDGMENTS.....	xiii
CHAPTER 1 INTRODUCTION.....	1
1.1 Overview of Current Renewable Energy.....	1
1.2 Sewer Drop Structure.....	4
1.3 Research Objective and Scope of Dissertation.....	7
1.4 Organization of Dissertation.....	8
CHAPTER 2 LITERATURE REVIEW.....	9
2.1 Traditional Energy from Wastewater System.....	9
2.2 Flow in a VDS.....	12
CHAPTER 3 DESIGN OF TURBINE FOR VOREX DROP STRUCTURES.....	17
3.1 Requirements for Turbine.....	17
3.2 Geometrical Parameters of Blade.....	20
CHAPTER 4 ANALYTICAL MODEL OF THE TURBINE.....	24
4.1 Introduction.....	24
4.2 Performance Characteristics.....	24
4.3 Implementation of Analytical Model.....	25

	vi
<b>CHAPTER 5 NUMERICAL MODEL OF THE TURBINE.....</b>	<b>29</b>
<b>5.1 Numerical Modeling of Flow within VDS.....</b>	<b>29</b>
<b>5.1.1 Single-Fluid Model.....</b>	<b>31</b>
<b>5.1.2 Two-Fluid Model.....</b>	<b>34</b>
<b>5.2 Numerical Model of Turbine.....</b>	<b>37</b>
<b>CHAPTER 6 EXPERIMENTAL WORK AND COMPARISON OF RESULTS WITH NUMERICAL AND ANALYTICAL SOLUTION.....</b>	<b>41</b>
<b>6.1 Liquid Flow through VDS.....</b>	<b>41</b>
<b>6.1.1 Experimental Setup-1.....</b>	<b>41</b>
<b>6.1.2 Results and Discussion.....</b>	<b>43</b>
<b>6.2 Turbine Performance.....</b>	<b>47</b>
<b>6.2.1 Experimental Setup-2.....</b>	<b>47</b>
<b>6.2.2 Measurement of Static Torque.....</b>	<b>50</b>
<b>6.2.3 Measurement of Dynamic Torque.....</b>	<b>50</b>
<b>6.2.4 Results and Discussion.....</b>	<b>52</b>
<b>6.3 Parametric Study of Turbine.....</b>	<b>62</b>
<b>6.3.1 Elevation.....</b>	<b>62</b>
<b>6.3.2 Optimization of Blade Angle.....</b>	<b>65</b>
<b>6.3.3 Optimization of Blade Width.....</b>	<b>67</b>
<b>6.3.4 Optimization of Blade Numbers.....</b>	<b>69</b>
<b>CHAPTER 7 CONCLUSION AND FUTURE WORK.....</b>	<b>72</b>
<b>7.1 Conclusion.....</b>	<b>72</b>
<b>7.2 Future Work.....</b>	<b>74</b>
<b>APPENDIX A AIR FLOW THROUGH VDS.....</b>	<b>75</b>



	vii
APPENDIX B EXAMPLE OF ANALYTICAL SOLUTION.....	82
BIBLIOGRAPHY.....	88

## LISTS OF FIGURES

<b>Figure 1-1:</b>	Different sources of U.S. energy production from 2003-2013.....	2
<b>Figure 1-2:</b>	U.S. electrical power carbon dioxide emission from 2005-2013.....	3
<b>Figure 1-3:</b>	Renewable energy generation in selected years, 2013-2040.....	4
<b>Figure 1-4:</b>	Diagram of an underground sewer system and location of the vertical drop shafts.....	5
<b>Figure 1-5:</b>	Photographs of VDS: (a) during installation, (b) top view and (c) side view.....	7
<b>Figure 2-1:</b>	Summary of energy opportunities from domestic wastewater.....	10
<b>Figure 2-2:</b>	Control volume of liquid in a vertical drop shaft.....	14
<b>Figure 3-1:</b>	(a) Radial-flow Francis turbine and (b) axial-flow Kaplan turbine.....	18
<b>Figure 3-2:</b>	Schematic diagram of (a) traditional turbine and (b) eVortex turbine.....	19
<b>Figure 3-3:</b>	Pictorial representation of eVortex with an integrated axial flux type electrical generator.....	20
<b>Figure 3-4:</b>	Schematic diagram of a single blade profile.....	20
<b>Figure 3-5:</b>	(a) Top surface of a blade and (b) CAD model of eVortex with blades.....	22
<b>Figure 4.1:</b>	Schematic diagram of a moving control volume over a blade.....	26
<b>Figure 5-1:</b>	(a) A small scale of a VDS installed at the Hydraulic Laboratory of Bogard Hall. (b) Close up view of the inlet.....	30
<b>Figure 5-2:</b>	Dimension (cm) of a small scale VDS.....	30
<b>Figure 5-3:</b>	Mesh of generation in the Flow3D.....	32
<b>Figure 5-4:</b>	Diagram of boundary conditions.....	33

<b>Figure 5-5:</b>	(a) CAD model of the inlet structure and the discretization by blockMesh. (b) The final discretization of the inlet structure in OpenFOAM.....	36
<b>Figure 5-6:</b>	Dimension (cm) of a larger scale VDS.....	38
<b>Figure 5-7:</b>	Up-close picture of mesh cells at (a) inlet structure and (b) turbine section (dimension in cm). (c) Mesh for the entire VDS.....	39
<b>Figure 5-8:</b>	Rotational speed of free to rotate versus number of cells in the model.....	40
<b>Figure 6-1:</b>	(a) Top and (b) side views of small scale vortex drop structure used in the experiment. (c) Water pump.....	42
<b>Figure 6-2:</b>	Diagram of (a) pressure transducer mounting position and (b) its measured location in each elevation. (c) Actual photo of the pressure transducer.....	42
<b>Figure 6-3:</b>	Contour of fluid fraction along the VDS from (a) two-fluid and (b) single fluid models.....	43
<b>Figure 6-4:</b>	Comparison of average wall pressure along the elevation from analytical, experimental and numerical (single-fluid and two-fluid) methods.....	44
<b>Figure 6-5:</b>	Comparison of average tangential ( $V_\theta$ ) and axial ( $V_z$ ) velocity along the elevation.....	45
<b>Figure 6-6:</b>	The cross-sectional pressure distribution of (a) two-fluid and (b) single-fluid model at the elevation of 0.5 m below the shaft entrance.....	46
<b>Figure 6-7:</b>	Comparison of pressure along radial axis at cross-section of 0.5 m below the shaft entrance between analytical and numerical results.....	47
<b>Figure 6.8:</b>	(a) Large scale VDS constructed at Trenchless Technology Center (TTC). (b) Diagram of water flow in the VDS.....	48
<b>Figure 6-9:</b>	(a) The diagram of eVortex turbine. (b) Side view and (c) top view of the actual eVortex turbine.....	49
<b>Figure 6-10:</b>	(a) Diagram and (b) actual installation of the load cell to measure the static torque.....	50

<b>Figure 6-11:</b>	(a) Diagram of the two pulleys transmission power system for measuring dynamic torque and speed. (b) Actual turbine with transmission during the calibration.....	51
<b>Figure 6-12:</b>	Calibration between input voltage of the magnetic brake and the calculated torque.....	52
<b>Figure 6-13:</b>	Velocity of water through VDS with turbine located at 5.64 m below the entrance.....	53
<b>Figure 6-14:</b>	Numerical result of rotational speed from starting to steady state.....	54
<b>Figure 6-15:</b>	Snapshots from simulations showing velocity of flow for various torque applied ((a) 0 Nm, (b) 0.5 Nm, (c) 1 Nm, (d) 1.5 Nm, and (e) 2 Nm). The corresponding speeds were (a) 465.53 rpm, (b) 348.17 rpm, (c) 241.02 rpm, (d) 153.01 rpm, and (e) 60.75 rpm.....	55
<b>Figure 6-16:</b>	The torque and power generated for 190 GPM using numerical model....	56
<b>Figure 6-17:</b>	Power available for elevations and flow rate.....	57
<b>Figure 6-18:</b>	Diagram between turbine speeds and flow rates from analytical, numerical and experimental results.....	58
<b>Figure 6-19:</b>	Static torques versus flow rates obtained from analytical and experimental methods .....	59
<b>Figure 6-20:</b>	Comparison of torque-speed from analytical solutions, numerical model and experiments at water flow rate of 190 GPM.....	60
<b>Figure 6-21:</b>	Comparison of power versus speed from analytical, numerical and experiment for flow rate of 190 GPM.....	62
<b>Figure 6-22:</b>	Numerical torque versus speed at various elevations.....	63
<b>Figure 6-23:</b>	Analytical torque versus speed at various elevations.....	63
<b>Figure 6-24:</b>	Power versus speed at various elevations.....	64
<b>Figure 6-25:</b>	Efficiency versus speed at various elevations.....	65
<b>Figure 6-26:</b>	CAD model of various blade angle ( $\alpha$ ): (a) 30 degrees, (b) 45 degrees, and (c) 60 degrees.....	65
<b>Figure 6-27:</b>	Numerical torque versus speed at various blade angles ( $\alpha$ ).....	66

<b>Figure 6-28:</b> Analytical torque versus speed at various blade angle ( $\alpha$ ).....	66
<b>Figure 6-29:</b> Power versus speed at various blade angles ( $\alpha$ ).....	67
<b>Figure 6-30:</b> CAD model of various blade width ( $W$ ): (a) 3.81 cm, (b) 2.54 cm, and (c) 1.27 cm.....	67
<b>Figure 6-31:</b> Numerical torque and speed at various blade widths ( $W$ ).....	68
<b>Figure 6-32:</b> Power and rotational speeds at various blade widths ( $W$ ).....	69
<b>Figure 6-33:</b> CAD model of various number of blades ( $N$ ): (a) three blades, (b) four blades, (c) five blades, and (d) six blades.....	69
<b>Figure 6-34:</b> Numerical torque versus speed as various number of blades ( $N$ ).....	70
<b>Figure 6-35:</b> Power versus speed at various number of blades ( $N$ ).....	71
<b>Figure A-1:</b> (a) Pressure transducer with rated maximum of 800 Pa and (b) Pitot tube using in the air measurement.....	76
<b>FigureA-2:</b> (a) Diagram and (b) actual photo of the air pressure measurement.....	77
<b>Figure A-3:</b> (a) Diagram and (b) actual photo of the velocity measurement.....	78
<b>Figure A-4:</b> The location of the shaft's outlet when (a) exposed to atmospheric air and (b) submerged in water in a pool.....	78
<b>Figure A-5:</b> Static pressure of air at the inlet structure.....	79
<b>Figure A-6:</b> Differential pressure data from Pitot tube.....	80

## LIST OF TABLES

<b>Table 1-1:</b>	U.S. energy production in 2013 by energy source.....	2
<b>Table 1-2:</b>	Summary of existing drop structures at selected locations.....	5
<b>Table 3-1:</b>	Geometrical parameters of eVortex prototype.....	21
<b>Table A-1:</b>	Comparison of air flow velocity from the numerical result and experiments.....	81
<b>Table B-1:</b>	Numerical result of average velocity at the shaft entrance.....	83

## **ACKNOWLEDGMENTS**

First, I would like to sincerely thank Dr. Arun Jaganathan, my advisor, for giving me an opportunity be part of his research project as well as funding support during my Ph.D. program. He provided me valuable experience, profound engineering knowledge, and comprehensive academic guidance to pursue my doctoral degree. Secondly, I would like to thank Dr. Erez Allouche who introduced me to the Trenchless Technology Center (TTC) and allowed me to be part of this wonderful research center. I would like to thank my committee members including Dr. Arun Jaganathan, Dr. Neven Simicevic, Dr. David Hall, Dr. Leland Weiss and Dr. Tom Iseley. They gave me constructive feedbacks and valuable suggestions during my oral comprehensive exam and dissertation defense. Finally, I would like to thank all the people of TTC, especially all the folks in TTC research facility at south campus who helped me with the research experiments.

I would like to thank my Thai friends, Thanadech Thanakornworakij, Phadungsak Phongphonkit, Narate Taerat, and Nichamon Naksinehaboon for their help and support.

I would also like to thank and dedicate this dissertation to my parents, Somnuk and Kusuma Chusilp and my dear sister, Sinobol Chusilp, for their unconditional love and for supporting me my whole life.

## CHAPTER 1

### INTRODUCTION

In this dissertation, an energy-harvesting device to extract kinetic energy from fluid flow within the vortex drop structures used in the sewer system is presented. In this chapter, an overview of renewable energy production related to the research topic is presented. Following the overview, a general introduction of the sewer drop structures is given. The objective and organization of the dissertation is also presented.

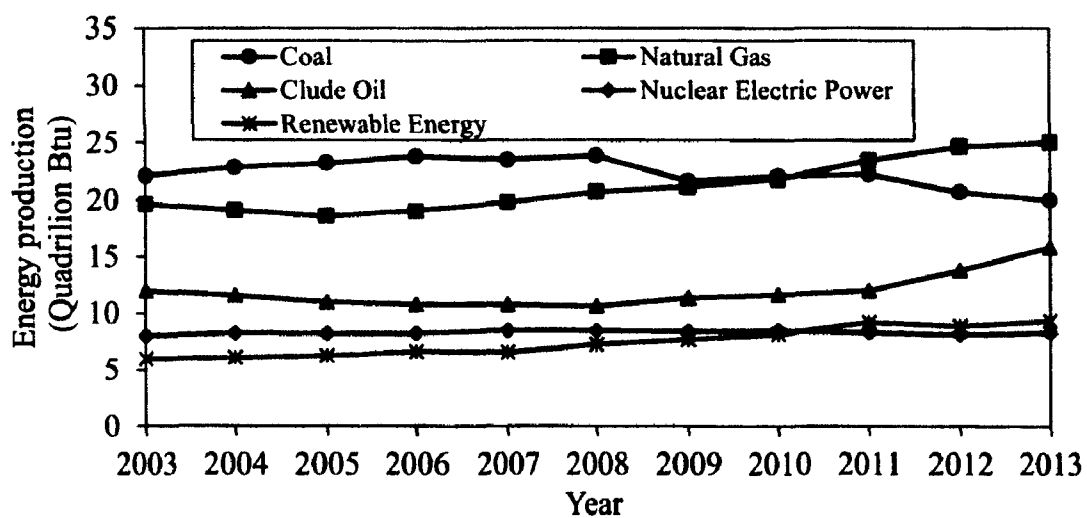
#### 1.1 Overview of Current Renewable Energy

Renewable energy resources including biomass, hydropower, geothermal, wind and solar are commonly used for energy production [1]. Based on the U.S. Information Administration [1], the majority of energy production comes from nonrenewable sources. During 2013, the total energy production from nonrenewable sources was about 72 quadrillion Btu which accounted for 89% of the total energy production in the U.S. (Table 1-1). Total energy generated from renewable sources was significantly lower. Its main sources was from biomass followed by hydroelectric power. Figure 1-1 shows a trend of the U.S energy production over the past decade [1]. The share of energy from renewable sources has been increasing steadily since 2003.



**Table 1-1: U.S. energy production in 2013 by energy source [1].**

Energy Source	Production (Quadrillion Btu)
<b>Nonrenewable</b>	
Coal	19.988
Natural gas	24.991
Crude oil	15.797
Natural gas plant liquids	3.601
Nuclear electric power	8.268
<b>Total</b>	<b>72.645</b>
<b>Renewable</b>	
Hydroelectric power	2.561
Geothermal	0.221
Solar/Photovoltaics	0.307
Wind	1.595
Biomass	4.614
<b>Total</b>	<b>9.298</b>
<b>Total Energy</b>	<b>81.943</b>

**Figure 1-1: Different sources of U.S. energy production from 2003-2013.**

Burning of fossil fuels such as coal in power plants generates a high amount of carbon dioxide gas which is linked to global warming [2]. Based on the U.S. Energy Information Administration [3], electricity generation from non-carbon resources, especially wind and solar, in 2013 could reduce carbon dioxide by about 150 million metric tons or around 20% of total carbon dioxide predicted using a fixed demand growth rate and carbon intensity at year 2005 (**Figure 1-2**).

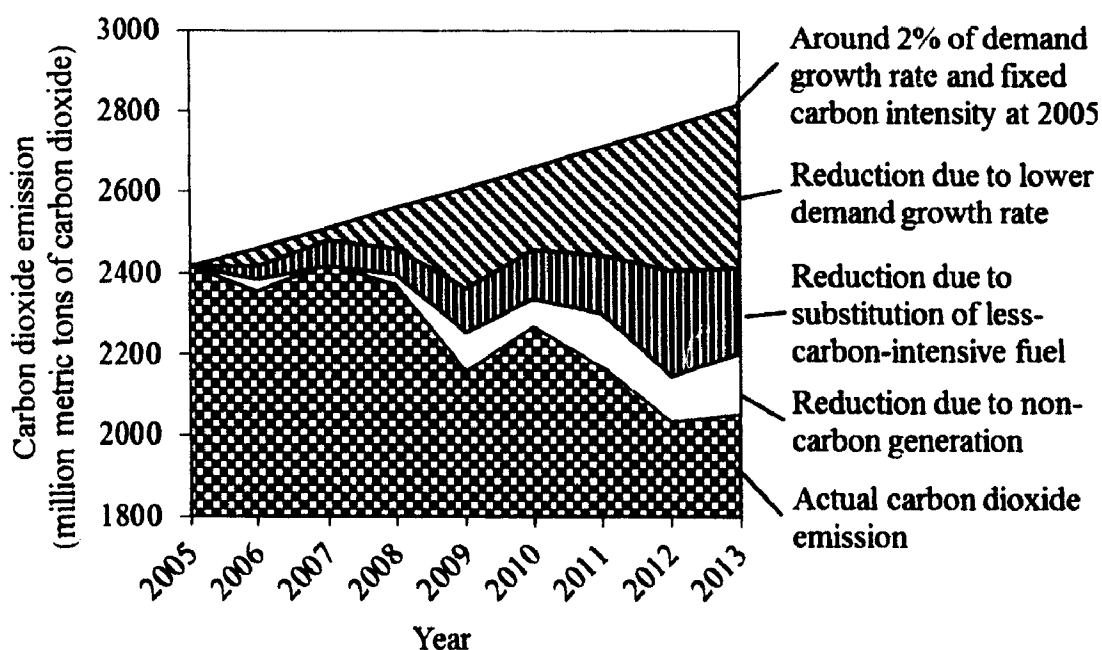


**Figure 1-2:** U.S. electrical power carbon dioxide emission from 2005-2013 [3].

Based on the U.S. Energy Information Administration [4], by the end of 2040, the total power generation (combined from both electric power and end-use sectors) from renewable energy resources is expected to be increased to about 909 billion kilowatt-hours, which is around 2% of the annual growth rate since 2013 (**Figure 1-3**). Solar energy has the highest annual growth rate followed by geothermal energy. Thus renewable energy resources play an important role in future energy production.

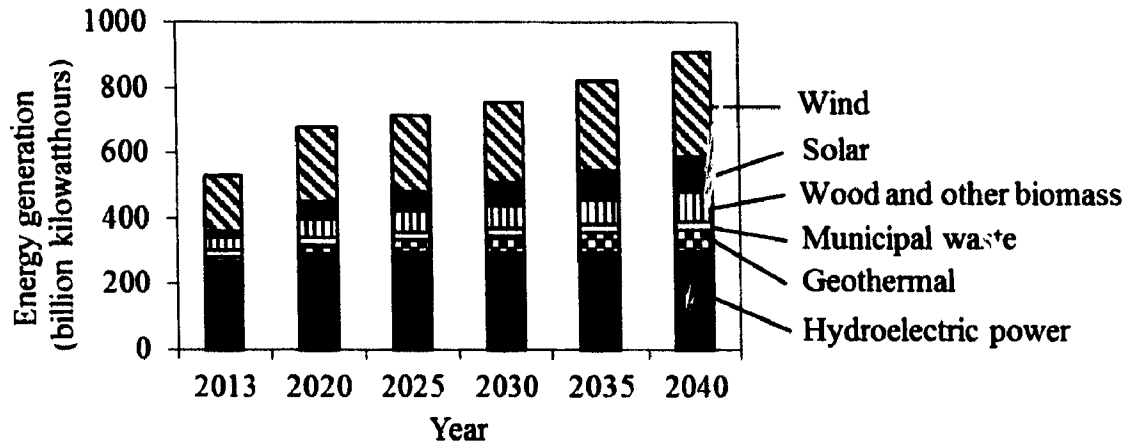


**Figure 1-3: Renewable energy generation in selected years, 2013-2040 [4].**

## 1.2 Sewer Drop Structure

The sewer drop structure is a vertical conduit in the sewer and storm water conveyance systems [5]. The drop structure consists of a vertical drop shaft where sewage flows from higher to lower elevation due to a change in ground topography.

**Figure 1-4** shows a picture of an underground sewer system with a sewer drop structure installed [6]. There are thousands of drop structures installed across the U.S. ranging from 2 m to over 100 m in height, carrying flow rates up to several million gallons per day. **Table 1-2** gives a summary of drop structures installed at selected locations across the world.

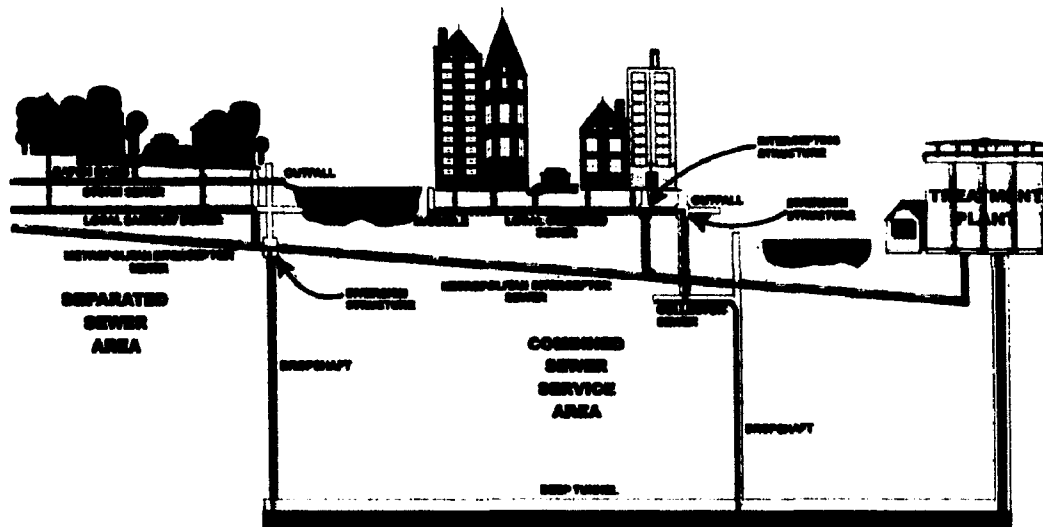


**Figure 1-4:** Diagram of an underground sewer system and location of the vertical drop shafts.

**Table 1-2:** Summary of existing drop structures at selected locations.

Location	Quantity	Depth (m)	Flow Rate (m <sup>3</sup> /s)
Chicago, IL	250	-	Up to 133
Milwaukee, WI	24	Up to 91	6 - 70
Pittsburgh, PA	165	Up to 27.5	-
Singapore	18	21 - 40	Up to 19.5
Montreal, Quebec	68	Up to 30	-
Toronto, Ontario	-	Up to 27.5	-
Phoenix, AZ	7	-	-
Rochester, NY	60	-	-
Minneapolis, MN	2	Up to 16	-
Sydney, Australia	Several	39.5 - 110	-
Cleveland, OH	12	Up to 61	Up to 6.5

Richmond, VA	Several	21	-
Dearborn, MI	3	-	-
Toledo, OH	Several	-	-
Austin, TX	Several	-	-
Dorchester, MA	6	-	-

In traditional drop structures called plunge drop structures, the incoming sewage falls freely from higher elevation to a lower elevation line through a vertical shaft [7]. The continuous pounding of free falling sewage against the concrete basement inside a plunge drop structure not only results in severe abrasive damage, but also the high turbulence within the fluid releases corrosive and odorous gases such as hydrogen sulfide (H<sub>2</sub>S), which eventually escapes into the atmosphere causing public health concerns. On the other hand, vortex drop structures (VDS) are specifically designed to mitigate odor and abrasion problems [8]. **Figure 1-5** shows pictures of a vortex drop structure [9].

A VDS consists of three main components: (a) an inlet section, (b) a vertical drop shaft, and (c) a mixing reservoir [10]. The incoming wastewater is directed and accelerated inside the inlet by a spiral pathway (**Figure 1-5(b)**). As passing through the vertical shaft, it maintains an air core at the center and follows a helix-like pattern (**Figure 1-5(c)**). Due to the swirling flow profile, the pressure inside the air core is slightly lower than the atmospheric pressure, and thus the air from outside is dragged into the shaft which traps the dissolved gasses from escaping into the atmosphere. The helical flow increases the travel path along the shaft and thus serves as energy dissipation through friction, minimizing the abrasive damages.

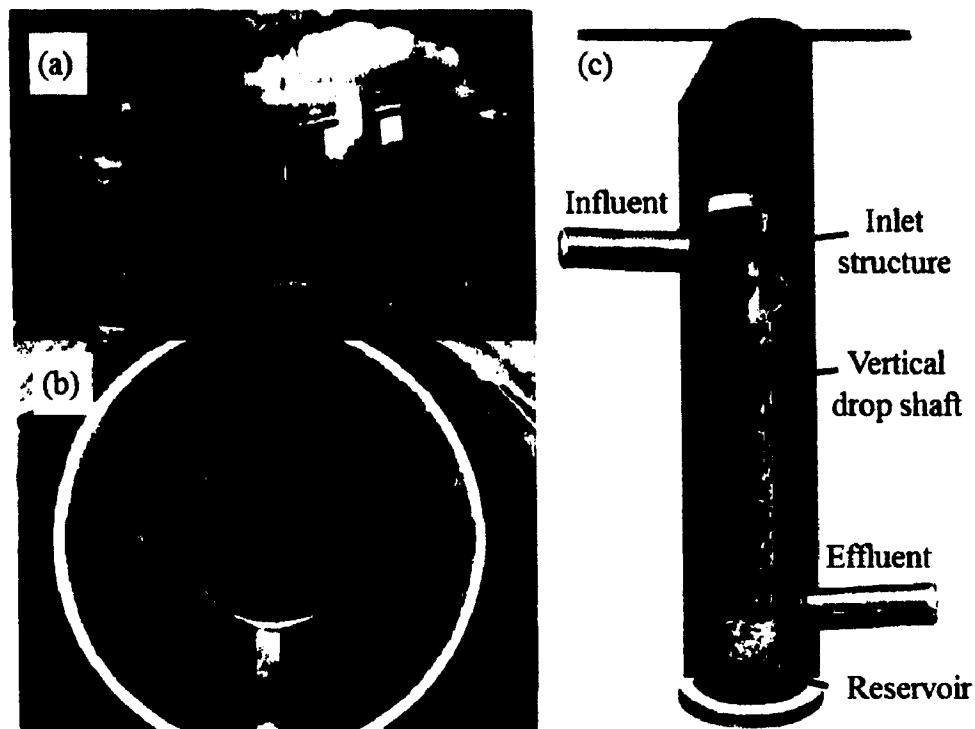


**Figure 1-5:** Photographs of VDS: (a) during installation, (b) top view and (c) side view.

Typically, a VDS is designed for a certain maximum flowrate depending upon several factors including topography. For example, a case study based in City of St. Robert, MO, a VDS with a shaft diameter about 30 cm, and a depth of 1.83 m was reported with peak flow of 2200 GPM [9]. The available power from the VDS was estimated at around 6 kilowatts (a calculation procedure will be described later in the dissertation). With the bigger size of the VDS and the higher flow rate, the increase of power availability could be expected.

### **1.3 Research Objective and Scope of Dissertation**

In this dissertation, an energy harvesting mechanism is developed to harvest the excessive kinetic energy using a custom designed water turbine (called eVortex) for

sewer VDS. Design and performance analysis of the turbine are the main focus of this work.

#### **1.4 Organization of Dissertation**

This dissertation is organized as follows: Chapter 2 presents a literature review on energy harvesting techniques available for wastewater system and analysis of flow in VDS. The overall concept of eVortex turbine and various design parameters are discussed in Chapter 3. Chapter 4 presents the theoretical analysis of the turbine. Chapter 5 presents the numerical modelling carried out to predict its performance. Chapter 6 presents the result from experimental work and comparison of measured data against analytical and numerical results. Finally, Chapter 7 provides summary and conclusion along with suggestions for future work.

## **CHAPTER 2**

### **LITERATURE REVIEW**

In this chapter, literature relevant to the dissertation is summarized. Literature review presented in this chapter is divided into the following sections: 1) review of the forms of energy available in wastewater and 2) review of the characteristic flow in VDS. Energy available from wastewater is harvested in several ways including chemical (solids and liquids compound), mechanical (hydraulics) and thermal (heat). Leading from the basic functions and configuration of typical VDS mentioned in the introduction, the characteristic flow analysis in the drop structures from other researchers are reviewed. Knowing the basic characteristics of the fluid flow in a VDS helps in the proper design of turbine and to predict its performance.

#### **2.1 Traditional Energy from Wastewater System**

Sewage was considered an alternative energy source which was primarily recovered at wastewater treatment plants [11]. It was discovered that raw wastewater potentially possessed energy around 10 times the electrical energy required for its treatment [12]. Thus, energy recovery from wastewater gains significance in order to achieve energy neutrality and sustainability in wastewater industry [13]. Various forms of energy are available from wastewater including chemical, thermal and mechanical. **Figure 2-1** shows a summary of energy opportunities from domestic wastewater [14].



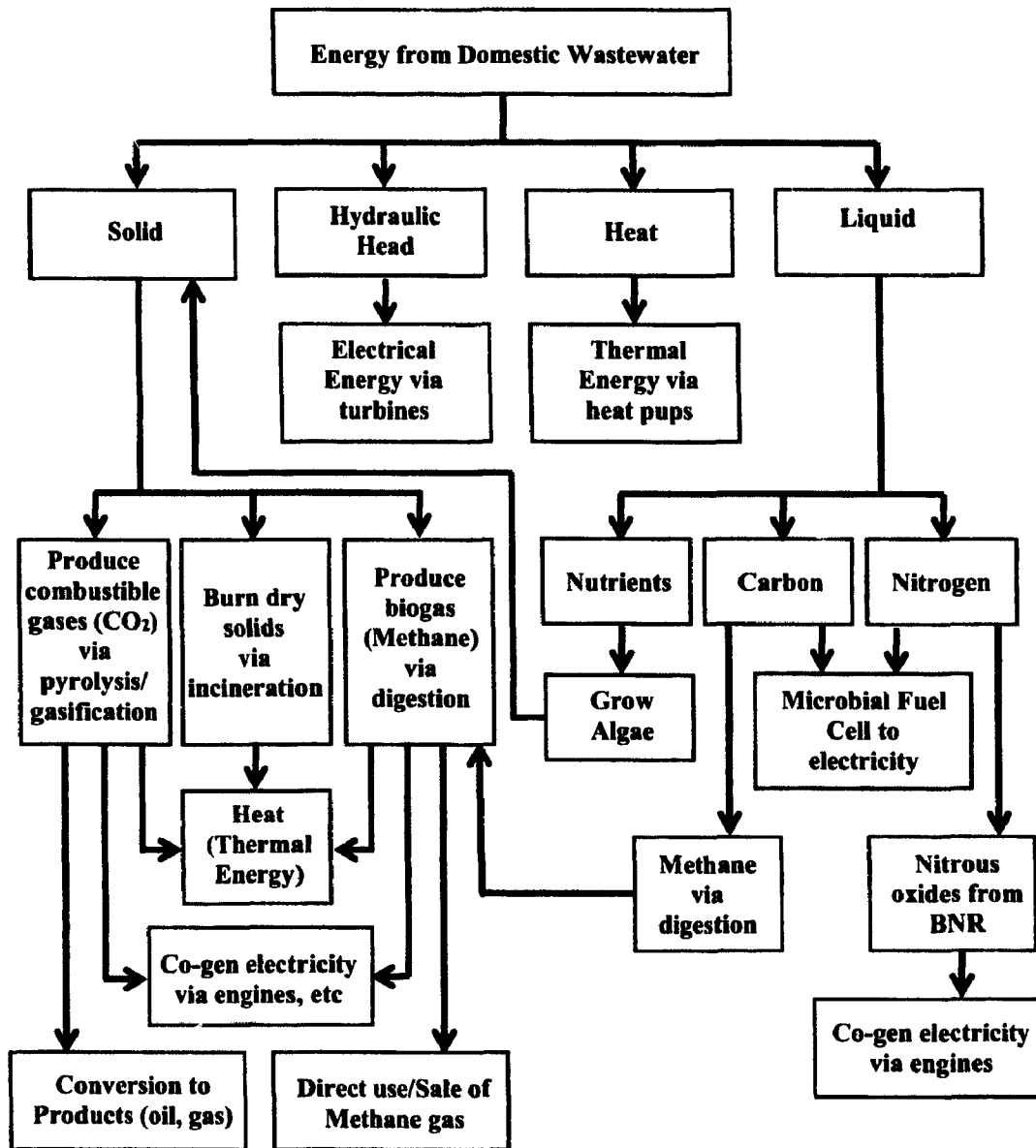


**Figure 2-1:** Summary of energy opportunities from domestic wastewater.

Chemical energy that exists in wastewater is mainly from organic matter. Organic matters are chemical compounds composed of carbon, hydrogen, oxygen, and other elements, and categorized into principal groups including proteins, 40-60%, carbohydrates, 25-50% and fats, 10% [15]. Biogas is produced from the organic matters via the use of anaerobic digestion. In sludge treatment process, anaerobic organisms are used to break down organic matter in the sewage in the absence of oxygen, and the

digestion additionally generates biogas which consist of methane (CH<sub>4</sub>) and carbon dioxide (CO<sub>2</sub>) as a by-product [16]. The methane from the treatment process may later be used in further energy transformation such as heat and electricity via cogeneration [17] and biomethane [18]. Biosolids or dry solids that are removed from the wastewater in the treatment process can be used to recover energy via incineration. Most common technologies used in the biosolid incineration system are Multiple Hearth Furnace (MHF) and Fluidized Bed Furnace (FBF) [19]. Although the biosolid incineration helps treatment plants effectively reduce the volume of solid waste and recover energy, it requires high amount of capital investment and requires fossil based fuel to operate [20]. Other technologies such as gasification [21] and pyrolysis [22] transform the solid waste into useful energy fuel via high temperature. Microbial fuel cells [23] and algae [24] was reported to extract energy from liquid in the sewage.

Thermal energy or heat could be captured from wastewater due to higher temperature. Typically the temperature of wastewater coming from household and industrial activities is warmer than the water supply [15]. Heat exchangers [25] and heat pump [26] were reported to recover heat from wastewater. New technologies involving thermoelectric, thermionic, and piezoelectric devices are still in development capable of transforming heat to electricity directly [27].

Mechanical energy from wastewater is available in terms of potential and kinetic energy. In wastewater treatment facilities, traditional low-head hydropower turbines are utilized to generate electrical power from treated effluents discharged [28]. Several wastewater treatment plants use hydropower turbine to harvest electrical power [29] [30] [31]. One example is the Point Loma Wastewater Treatment Plant in San Diego,

California [29]. It has a hydroelectric plant to harvest energy from treated wastewater discharged through 4.5 miles of ocean outfall connected after a 90-ft drop from the plant to the ocean. It was reported that this plant could generate power of 1350 kW from the wastewater which was later supplied to the San Diego electric grid. This amount of electricity is capable of feeding into about 1300 household residents.

Several water turbine based mechanisms have been reported in the past to extract kinetic energy from municipal pipelines operating under partial and full flow conditions. A paddle wheel like micro turbine that can be installed within a manhole of gravity sewer have been reported [32]. Lucid Energy has developed a Water-to-Wire system using spherical vertical axis turbine for potable water pipes [33]. Benkatina hydroelectric turbine is another available device for harvesting energy from freshwater and wastewater pipelines [34].

## **2.2 Flow in a VDS**

Several studies describing various aspects of a VDS including flow characteristics, air intake and odor removal are found in the literature, and most of those studies are based on the analytical and experimental modeling approach. Several types of inlet structures were investigated for drop structures including spiral type [35] and tangential type [36]. Various flow characteristics through the inlet structure including the relationship between discharge and hydraulic head [37] [38] [39], relationship between discharge and depth [40] [41], size of the air core [41] [42], and hydraulic jumps occurring inside the inlet structure [42] were studied analytically. Closed form solutions for various characteristics inside the spiraling flow including pressure distribution [43] [44], velocity of water [10] [43] [44] [45] and thickness of the water layer [43] [44] were

developed and validated against experimental measurements. Also, the performance characteristics of the VDS including the energy dissipation rate and the air entrainment were also studied and empirically relationships were formulated [43] [44].

In the vertical drop shaft, the liquid flow velocity mainly consists of two components including axial and tangential. These velocities create an empty region at the center while leaving the fluid to flow in helical-like patterns near the shaft wall. Quick [46] did experimental investigation of tangential velocity flow of the drop shaft and noticed that in any cross-sectional area the circulation ( $\Omega$ ) is constant. The circulation was estimated using the following:

$$\Omega = v_{\theta} r, \quad \text{Eq. 2-1}$$

where  $v_{\theta}$  is the tangential velocity and  $r$  is the radial coordinate of the flow. This curvature flow pattern is called the “free vortex” [47].

The actual liquid flow in the drop shaft is three-dimensional with turbulence. It is complicated to derive an exact solution. Therefore, several assumptions are required to simplify the solution. Jain [43] presented an analytical model of a gradual swirling flow based on control volume analysis using the assumptions that 1) the control volume is axisymmetric, 2) tangential velocity distribution is satisfied in Eq. 2-1, 3) axial velocity of the liquid is constant over the cross-sectional area, and 4) the radial velocity component is zero. Therefore, the governing equations including continuity, vertical momentum and angular momentum are given as:

$$Q = A v_z, \quad \text{Eq. 2-2}$$

$$\frac{d}{dz} \left( Q v_z + \frac{F_p}{\rho} \right) = gA - \frac{\pi D \tau_z}{\rho}, \quad \text{Eq. 2-3}$$

$$\frac{d(Q\Omega)}{dz} = -\frac{\pi D^2 \tau_\theta}{2\rho}, \quad \text{Eq. 2-4}$$

where  $Q$  is the volume flow rates,  $A$  is the cross-sectional flow area,  $v_z$  is the axial velocity,  $F_p$  is the pressure force in the vertical direction,  $\rho$  is density,  $g$  is the gravitational acceleration,  $D$  is the diameter of the drop shaft,  $\tau_z$  is the vertical component of shear stress at the wall,  $\tau_\theta$  is the tangential component of the shear stress at the wall, and  $z$  is the elevation. The vertical pressure force in Jain's solution is neglected [43].

Following Jain [43], Zhao *et al.* [44] implemented the effect of the force pressure ( $F_p$ ) on the swirling flow model and validated its results with water flow in an actual vortex drop structure. Figure 2-2 shows the implemented control volume [44].

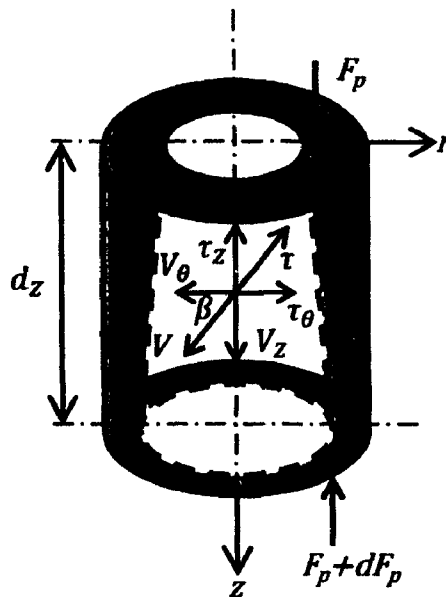


**Figure 2-2:** Control volume of liquid in a vertical drop shaft.

They assumed that the pressure distribution in a cross-sectional flow area is induced only by the centrifugal force. The pressure distribution ( $p$ ) equation is given as:

$$\int_{p_a}^p dp = \int_{R-b}^r \rho \frac{v_\theta^2}{r} dr. \quad \text{Eq. 2-5}$$

By letting the pressure  $p_a$  at the interface to be zero (gauge pressure), Eq. 2-5 can be written as:

$$p = \frac{1}{2} \rho \Omega^2 \left[ \frac{1}{R^2(1-t)^2} - \frac{1}{r^2} \right], \quad \text{Eq. 2-6}$$

where  $t = b / R$  is relative thickness, and  $b$  is water thickness measured from the interface to the wall. The pressure force ( $F_p$ ) is calculated from Eq. 2-6 as:

$$F_p = \int_{R-b}^R 2\pi p r dr = \frac{1}{2} \pi \rho \Omega^2 \left[ \frac{1}{(1-t)^2} + 2 \ln(1-t) - 1 \right]. \quad \text{Eq. 2-7}$$

By the given shear stress components  $\tau_z = \tau \sin \beta$  and  $\tau_\theta = \tau \cos \beta$  where  $\tau = \frac{1}{8} f \rho V^2$ ,  $f$  is the friction factor,  $V$  the average total velocity, and  $\beta$  is the angle between the average velocity components  $V$  and  $V_\theta$ . The new governing equations [44] were given as:

$$\frac{d\Omega}{dz} = -\frac{f\pi D^2}{16Q} V V_\theta, \quad \text{Eq. 2-8}$$

$$\frac{dV_z}{dz} = \left[ \frac{g}{V_z} - f \frac{\pi D V V_z}{8Q} (1-M) \right] / (1-T), \quad \text{Eq. 2-9}$$

$$M = \frac{1}{2t \tan^2 \beta} \left[ \frac{1}{(1-t)^2} + 2 \ln(1-t) - 1 \right], \quad \text{Eq. 2-10}$$

$$T = \frac{t(2-t)^3}{8 \tan^2 \beta (1-t)^4}, \quad \text{Eq. 2-11}$$

where the average tangential velocity  $V_\theta$  and the average axial velocity  $V_z$  are calculated

as:

$$V_\theta = \frac{1}{A} \int_{R-b}^R \tau_\theta \pi r dr = \frac{4\Omega}{(2-t)D}, \quad \text{Eq. 2-12}$$

$$V_z = \frac{Q}{A} = \frac{4Q}{\pi D^2 t (2-t)}. \quad \text{Eq. 2-13}$$

By knowing the pressure at the wall, water thickness, and initial conditions such as the flow rate and friction factor, Zhao *et al.* [44] predicted the flow condition from the above equations by using the numerical method. The above equation is valid only if  $M < 1$  and  $T < 1$ .

By knowing the flow characteristic from the above equations, the specific energy head ( $E$ ) and the total head ( $H$ ) are predicted using the following equations for elevation ( $Z$ ):

$$E = \frac{V_z^2}{2g} + \frac{2\Omega^2}{gD^2(1-t)^2}, \quad \text{Eq. 2-14}$$

$$H = E + Z. \quad \text{Eq. 2-15}$$

## **CHAPTER 3**

### **DESIGN OF TURBINE FOR VORTEX**

#### **DROP STRUCTURES**

In this chapter, an overview of the turbine for a VDS is presented. The turbine named “eVortex” was designed to be inserted along the vertical shaft of the VDS. Preliminary design as well as the geometric requirements are given in this chapter.

#### **3.1 Requirements for Turbine**

Traditional water turbines such as Francis and Kaplan are generally designed to be operated at full flow conditions found in applications including hydroelectric power generation or energy harvested from pressure pipes. The rotor is typically aligned at the center of the pipe with blades extruding toward the wall leaving a gap between two surfaces. **Figure 3-1** shows typical designs of a radial-flow Francis turbine and an axial-flow Kaplan turbine [47].



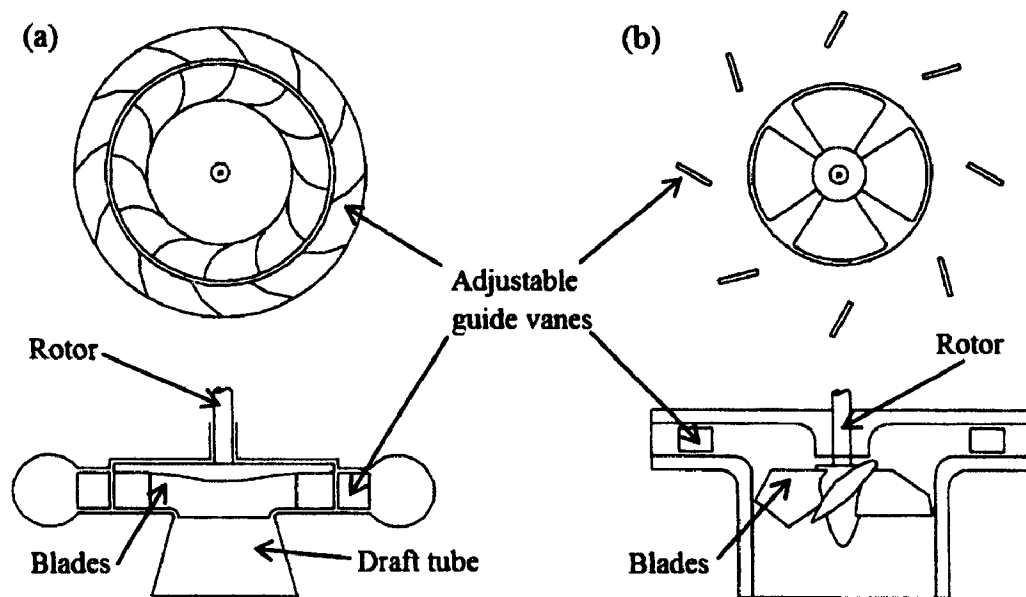


**Figure 3-1:** (a) Radial-flow Francis turbine and (b) axial-flow Kaplan turbine.

Although traditional turbines might be applied to any existing VDS, it would be less effective due to the type of flow in the VDS. In a VDS liquid occupies only a thin layer adjacent to the pipe wall leaving a major portion of the pipe empty. Thus, by retrofitting traditional turbines, only a partial amount of incoming fluid would strike the blades. Further blockage due to accumulation of debris or solid waste is another issue which would lead to frequent malfunction. The turbine placed at the center would reduce the performance of the drop structure itself. Thus, a new turbine design is required to effectively harvest the kinetic energy without compromising the original purpose of the VDS.

The geometry of eVortex turbine was designed to perform adequately under the swirling flow without interfering in a VDS's original function. The newly designed turbine consists of radial arrangement of blades attached to the inner wall of the pipe which is free to rotate. The blades are designed to intersect major portions of the flow.

The center core of the turbine is left open for air and other debris to pass through freely. It is expected that blockage due to debris would be minimal because of this open nature of the design. **Figure 3-2** shows the schematic of eVortex in comparison with a traditional turbine. As seen in **Figure 3-2**, the blades of eVortex are located where the flow is maximum. The section of the pipe containing the turbine is allowed to rotate freely via bearings.

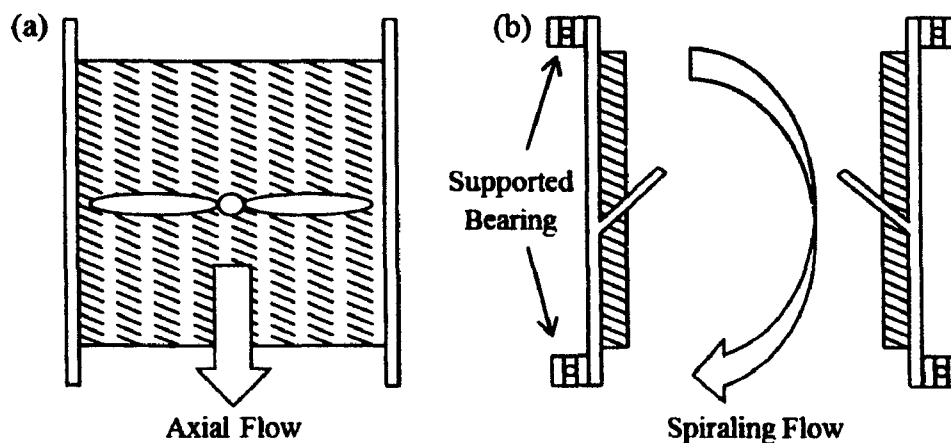


**Figure 3-2:** Schematic diagram of (a) traditional turbine and (b) eVortex turbine.

In a traditional turbine, torque is typically transferred using mechanisms involving gears and shafts to the electrical generator, and this mechanism increases the complexity and energy loss due to friction. To overcome these drawbacks, in eVortex the rotating pipe serves as rotor of the electrical generator which move magnets over statically placed coils (stator). **Figure 3-3** shows principal representation of the turbine integrated with an axial flux generator. This dissertation focuses only on the turbine design and the electrical generator is beyond the scope.

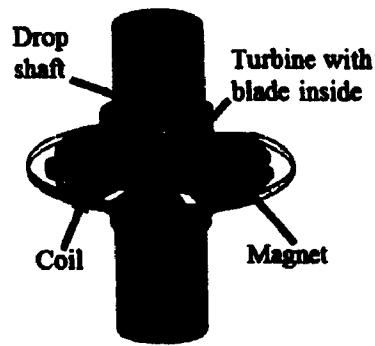


**Figure 3-3:** Pictorial representation of eVortex with an integrated axial flux type electrical generator.

### 3.2 Geometrical Parameters of Blade

The blade of the turbine was designed using helical geometry. **Figure 3-4** shows the schematic diagram of the blade along with various geometrical parameters. The parameters include height ( $H$ ), width ( $W$ ), blade angle ( $\alpha$ ) at the drop shaft radius ( $R$ ), number of blades ( $N$ ), and elevation ( $Z$ ) at which the turbine is placed along the shaft. A parametric study was undertaken to optimize the parameters for optimal energy extraction using numerical modeling. The results are presented in Chapter 6.

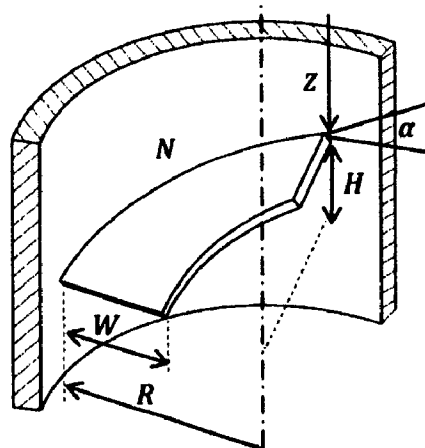


**Figure 3-4:** Schematic diagram of a single blade profile.

The coordinates of a point on the surface of the blade are given by the following parametric equations:

$$x = r \sin\left(\frac{h}{R \tan \alpha}\right), \quad \text{Eq. 3-1}$$

$$y = r \cos\left(\frac{h}{R \tan \alpha}\right), \quad \text{Eq. 3-2}$$

$$z = h, \quad \text{Eq. 3-3}$$

where  $0 \leq h \leq H$  and  $R - W \leq r \leq R$ . **Table 3-1** provides values for the geometrical parameters used for the prototype developed in this work. **Figure 3-5** shows the top surface of each blade and the CAD model of the turbine with four blades.

**Table 3-1:** Geometrical parameters of eVortex prototype.

Parameters	Value
Height ( $H$ )	11.92 cm
Width ( $W$ )	3.81 cm
Blade angle ( $\alpha$ )	45 degree
Drop shaft radius ( $R$ )	7.62 cm
Number of blades ( $N$ )	4 blades

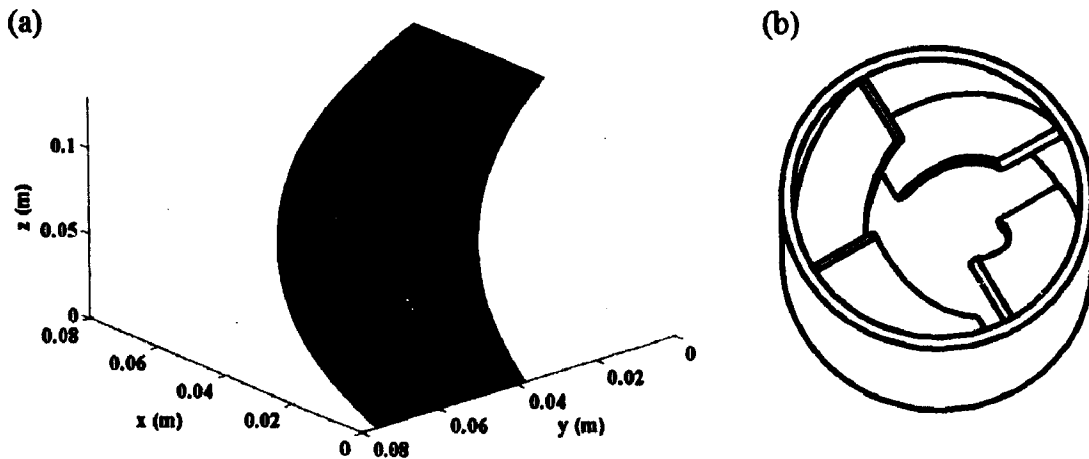


**Figure 3-5:** (a) Top surface of a blade and (b) CAD model of eVortex with blades.

A minimum number of blades required so that entire incoming fluid will intersect with the blades was determined by geometry of the turbine and incoming flow characteristics. Velocity ( $V$ ) could be resolved into axial ( $V_z$ ) and tangential ( $V_\theta$ ) components and let the incoming flow approach with angle ( $\beta$ ) (Figure 3-6).

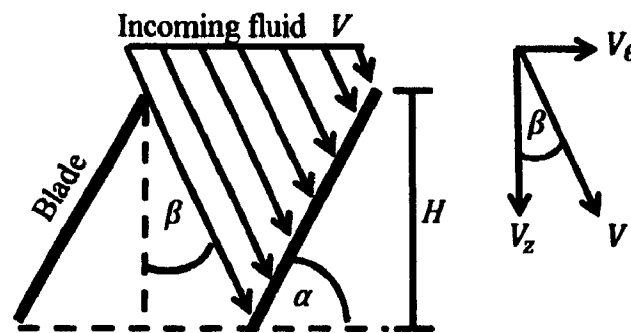


**Figure 3-6:** Diagram showing the angle of the incoming flow with respect to the blades.

Knowing blade height ( $H$ ) and angle ( $\alpha$ ), the minimum number of blades ( $N$ ) was determined by:

$$N \geq \frac{2\pi R \tan \alpha}{H(1 + \tan \alpha \tan \beta)} \quad \text{Eq. 3-4}$$

If the flow is unknown, the number of blades ( $N$ ) could be estimated by assuming

$\beta = 0$  (vertical drop):

$$N \geq \frac{2\pi R \tan \alpha}{H}. \quad \text{Eq. 3-5}$$

## **CHAPTER 4**

### **ANALYTICAL MODEL OF THE TURBINE**

In this chapter, analytical prediction of the performance of the turbine is presented. Analytical model was carried out using the finite control volume analysis method.

#### **4.1 Introduction**

In an actual scenario, the fluid flow through eVortex turbine is complicated, resulting in an unsteady flow with turbulence. When fluid approaches the blade, it spreads over the blade's surface area flowing in the direction depending on its profile. Major portion of fluid passes through lower portion of a blade.

#### **4.2 Performance Characteristics**

Flow problems are generally analyzed applying: 1) Conservation of mass, 2) Newton's Law of Motion, and 3) Conservation of Energy principles. Finite control volume analysis is a possible technique to determine flow behavior.

Main parameters that characterize a turbomachine include input and output power, and speed and efficiency. In a turbine, performance is typically expressed in term of head, speed, power developed at the shaft, efficiency, and the discharge flow rate [48]. The aim of the analytical solution presented in this chapter is to identify the torque generated ( $\tau$ ) and power ( $P$ ) for the given flow rate.

### 4.3 Implementation of Analytical Model

Flow over a blade was assumed to behave similarly to a fluid jet striking an inclined plane where a major portion of the flow exists near the wall such that it could be treated as one-dimensional.

In order to simplify the problem, the following assumptions are made: 1) flow is smooth with viscous effects neglected, 2) flow is considered steady, 3) radial component of fluid velocity is negligible, and 4) potential energy due to gravity is considered to be much lower than kinetic energy, so it could be neglected.

An inertial and nondeforming control volume is assigned over a blade as shown in **Figure 4-1**. Both control volume and the blade rotate together with specific angular velocity ( $\omega$ ) so their tangential velocity ( $\bar{U}$ ) could be defined at the location. While the turbine is spinning, incoming fluid enters the control volume with relative velocity  $\bar{W}_1$  and mass flow rate  $\dot{m}_1$ . After hitting the blade the flow separates into two directions with relative velocities  $\bar{W}_2$  and  $\bar{W}_3$  as shown in **Figure 4-1**. As the effect of gravity is neglected, the fluid is assumed to flow tangential to the blade. The relative velocity  $\bar{W}_1$  is given by **Eq. 4-1** as:

$$\bar{W}_1 = \bar{V}_1 - \bar{U} = V_{z1} \hat{e}_z + (V_{\theta 1} - \omega R) \hat{e}_\theta, \quad \text{Eq. 4-1}$$

where  $V_{z1}$  and  $V_{\theta 1}$  are axial and tangential components of the incoming fluid velocity ( $\bar{V}_1$ ). The relative velocity is also expressed in term of the velocity magnitude ( $W_1$ ) and its direction with angle ( $\beta$ ) as shown in **Eq. 4-2**:

$$\bar{W}_1 = W_1 \cos \beta \hat{e}_z + W_1 \sin \beta \hat{e}_\theta, \quad \text{Eq. 4-2}$$



where

$$W_1 = \sqrt{V_{z1}^2 + (V_{\theta1} - \omega R)^2}, \quad \text{Eq. 4-3}$$

$$\beta = \tan^{-1} \frac{V_{\theta1} - \omega R}{V_{z1}}. \quad \text{Eq. 4-4}$$

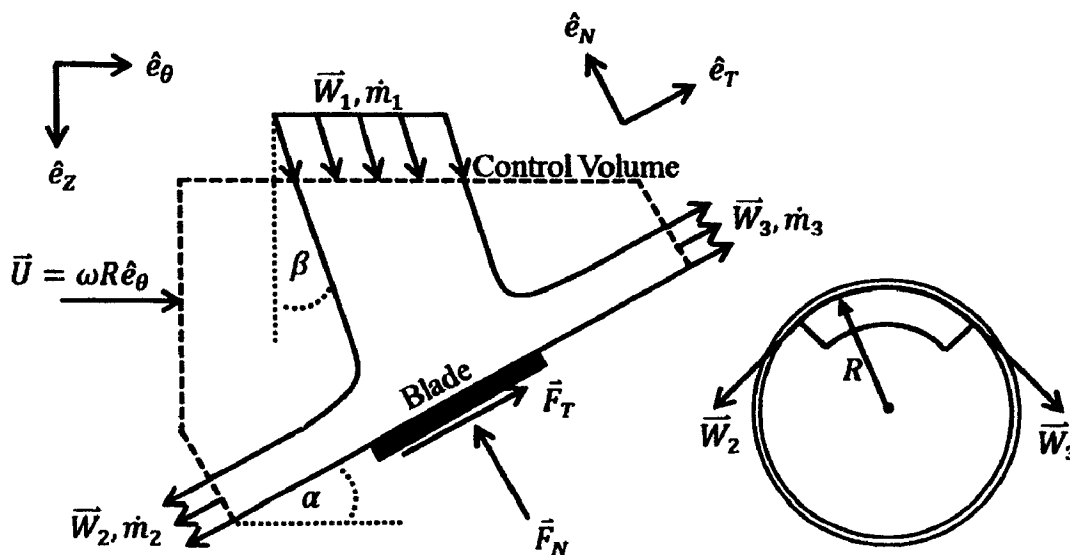


**Figure 4.1:** Schematic diagram of a moving control volume over a blade.

The external force ( $\vec{F}$ ) acting on the system could be determined applying Newton's second law to the finite control volume resulting in the following equation [47]:

$$\int_{cs} \vec{W} \rho \vec{W} \cdot \hat{n} dA = \sum \vec{F}. \quad \text{Eq. 4-5}$$

Summing up the external forces in normal ( $\vec{F}_N$ ) and tangential ( $\vec{F}_T$ ) directions is expressed in the following equation:

$$\sum \vec{F} = \vec{F}_N + \vec{F}_T = F_N \hat{e}_N + F_T \hat{e}_T. \quad \text{Eq. 4-6}$$

The individual variable on the left side of Eq. 4-5 are given as:

$$\vec{W}_1 = -W_1 \cos(\beta - \alpha) \hat{e}_N + W_1 \sin(\beta - \alpha) \hat{e}_T, \quad \text{Eq. 4-7}$$

$$\vec{W}_2 = -W_2 \hat{e}_T, \quad \text{Eq. 4-8}$$

$$\vec{W}_3 = W_3 \hat{e}_T, \quad \text{Eq. 4-9}$$

$$\hat{n}_1 = \cos \alpha \hat{e}_N + \sin \alpha \hat{e}_T, \quad \text{Eq. 4-10}$$

$$\hat{n}_2 = -\hat{e}_T, \quad \text{Eq. 4-11}$$

$$\hat{n}_3 = \hat{e}_T. \quad \text{Eq. 4-12}$$

Considering the mass flow rate at inlet ( $\dot{m}_1 = W_1 A_1 \cos \beta$ ) and outlet ( $\dot{m}_2 = \rho W_2 A_2$ ,  $\dot{m}_3 = \rho W_3 A_3$ ), the Eq. 4-5 could be solved as:

$$F_N = \dot{m}_1 W_1 \cos(\beta - \alpha), \quad \text{Eq. 4-13}$$

$$F_T = -\dot{m}_1 W_1 \sin(\beta - \alpha) - \dot{m}_2 W_2 + \dot{m}_3 W_3. \quad \text{Eq. 4-14}$$

By conservation of energy within the control volume, it can be defined that the magnitude of relative velocity ( $W$ ) remained constant, such that:

$$W_1 = W_2 = W_3. \quad \text{Eq. 4-15}$$

Because of conservation of mass,

$$\dot{m}_1 = \dot{m}_2 + \dot{m}_3. \quad \text{Eq. 4-16}$$

Using Eq. 4-15 and Eq. 4-16, Eq. 4-14 could be written as:

$$F_T = \dot{m}_1 W_1 [1 - \sin(\beta - \alpha)] - 2\dot{m}_2 W_1. \quad \text{Eq. 4-17}$$

$F_N$  (Eq. 4-13) could be solved directly, while  $F_T$  (Eq. 4-17) could not be solved because of the unknown mass flowrate ( $\dot{m}_2$ ). However, the external tangential force ( $F_T$ ) could be interpreted as frictional force along the surface with a low value compared to the normal force ( $F_N$ ). Therefore, for simplicity, the problem was assumed to be frictionless ( $F_T = 0$ ).

Additional mass flow rate ( $\dot{m}_2$ ) could also be determined as:

$$\dot{m}_2 = \frac{1}{2} \dot{m}_1 [1 - \sin(\beta - \alpha)]. \quad \text{Eq. 4-18}$$

$\vec{F}_N$  could be described in global coordinated ( $z, \theta$ ) as:

$$\vec{F}_N = -F_N \cos \alpha \hat{e}_z - F_N \sin \alpha \hat{e}_\theta. \quad \text{Eq. 4-19}$$

The torque ( $\tau$ ) generated is given as:

$$\tau = -F_N R \sin \alpha. \quad \text{Eq. 4-20}$$

Using Eq. 4-3 and Eq. 4-13, the torque can be expressed as:

$$\tau = -\dot{m}_1 R \sqrt{V_{z1}^2 + (V_{\theta1} - \omega R)^2} \cos(\beta - \alpha) \sin \alpha. \quad \text{Eq. 4-21}$$

Based on the analytical flow model by Zhou *et al.* [44], the axial velocity ( $V_z$ ) and circulation ( $\Omega$ ) for a cross section with the VDS were assumed to be constant. By estimating  $\Omega$  and  $V_z$  (Solve Eq. 2-8 and Eq. 2-9) for a given length along the VDS where the turbine is installed, the torque could be found using:

$$\tau = -\rho Q \sqrt{(RV_z)^2 + (\Omega - \omega R^2)^2} \cos(\beta - \alpha) \sin \alpha, \quad \text{Eq. 4-22}$$

where

$$\beta = \tan^{-1} \frac{\Omega - \omega R^2}{RV_z}. \quad \text{Eq. 4-23}$$

Power ( $P$ ) could be calculated by the following relationship:

$$P = \omega \tau. \quad \text{Eq. 4-24}$$

The results obtained using these equations are presented in Chapter 6 where they are compared against experimental and numerical data. A full calculation of an example problem is presented in Appendix B.

## CHAPTER 5

### NUMERICAL MODEL OF THE TURBINE

In this chapter, numerical analysis based on computational fluid dynamics (CFD) is presented. To numerically predict the performance of the turbine, simulations were carried out in two stages. In the first stage, the fluid flows through the VDS alone was studied. In the second stage, the turbine model was implemented within the drop shaft, and various parametric studies have been carried out to optimize the shape of the turbine for optimal energy harvesting.

#### 5.1 Numerical Modeling of Flow within VDS

Due to the literature, only a limited number of CFD-based investigations of VDS are reported [49] [50] [51]. Understanding flow patterns within the VDS based on the CFD is crucial. The numerical results were verified by comparing it with experiments and analytical results.

A small scale commercial VDS consisted of a spiral inlet structure and a drop shaft with a diameter of 10 cm and a height of 1 m was used as the test case for validating the model in the first stage (**Figure 5-1**). The structure could handle flow rates up to 10 liters per second. **Figure 5-2** shows the dimensions of the VDS used in stage 1.

Numerical analysis was carried out using two separate models. In the first model, only the flow of water (without air intake) was considered using a single-fluid theory. In

the second model, the flow of both water and air was considered simultaneously using a two-fluid theory.

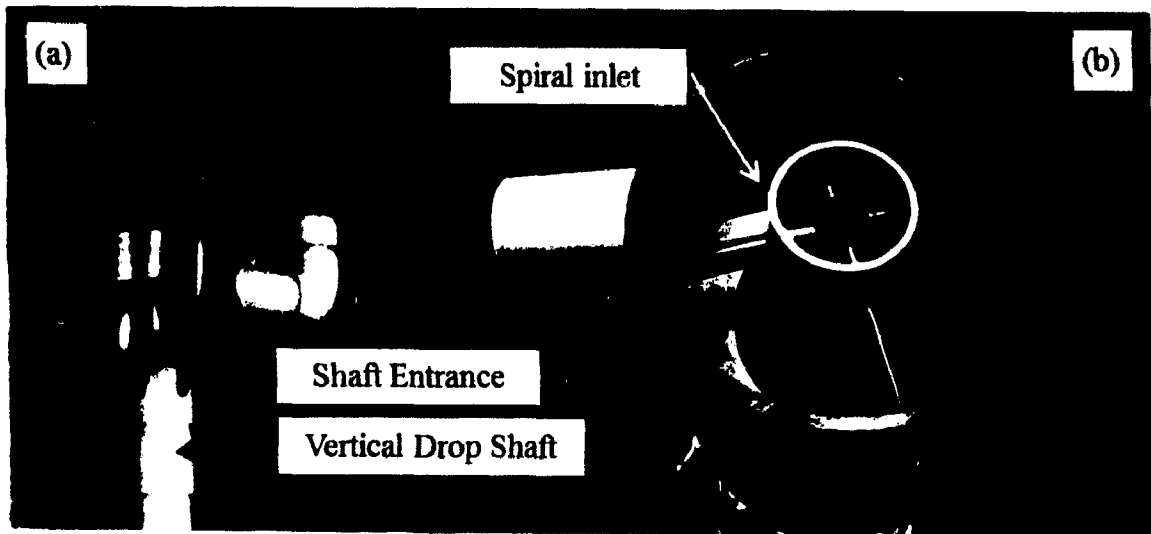


**Figure 5-1:** (a) A small scale of a VDS installed at the Hydraulic Laboratory of Bogard Hall. (b) Close up view of the inlet.

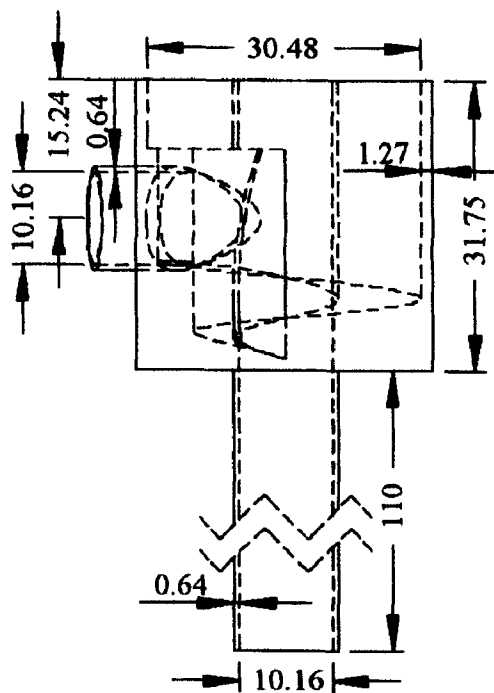


**Figure 5-2:** Dimension (cm) of a small scale VDS.

### 5.1.1 Single-Fluid Model

The single-fluid model was created using the commercial CFD package Flow3D [52]. In this model, only the liquid was involved, while the air portion was assigned as a void region. The governing equations for this model consists of the continuity and the Reynolds-average Navier-Stokes (RANS) equations. The modified FAVOR versions of the two equations [52] are given as:

$$\frac{\partial}{\partial X_i} (U_i A_i) = 0, \quad \text{Eq. 5-1}$$

$$\frac{\partial U_i}{\partial t} + \frac{1}{V_F} \left( U_j A_j \frac{\partial U_i}{\partial X_j} \right) = -\frac{1}{\rho} \left( \frac{dp}{dX_i} \right) + g_i + \frac{1}{\rho V_F} \left\{ \frac{\partial}{\partial X_j} (A_j \tau_{ij}) \right\}. \quad \text{Eq. 5-2}$$

The parameters  $i$  and  $j$  are the Einstein's summation variable with  $i, j = 1, 2$  and  $3$  corresponding to  $x, y, z$  in the Cartesian coordinate system,  $U$  is the velocity components,  $A$  is fractional area open to flow,  $V_F$  is the volume fraction of the fluid in each cell,  $\rho$  is the density of the fluid,  $p$  is pressure,  $g$  is body acceleration, and  $\tau$  is the Reynolds stress component. The Reynolds stress component was calculated following the two-equation turbulence model of the renormalization group (RNG k- $\epsilon$  model) [53]. RNG k- $\epsilon$  model is suggested to be suitable for swirling flows and flows with varying Reynolds numbers for different areas compared to the standard k- $\epsilon$  turbulence model [54].

The free surface of the fluid was handled using the volume of fluid (VOF) method [55]. The VOF uses the same procedure as FAVOR to determine the fluid function ( $F$ ) in each mesh cell. The fluid fraction of one corresponds to the cell occupied by liquid while zero corresponds to the void region. Cell with partially occupied by the fluid will have a

fluid fraction between zero and one. An additional transportation equation with a fluid fraction is required and is given by the following equation:

$$\frac{\partial F}{\partial t} + \frac{1}{V_F} \left[ \frac{\partial}{\partial X_i} (F A_i U_i) \right] = 0. \quad \text{Eq. 5-3}$$

The CAD model of the VDS was created and meshed. As the geometry consists of sharp edges, size of the cells should be fine enough to ensure accuracy and prevent the “stair-stepping” effects [52] which occur in coarse meshed models. Four rectangular boxes of Cartesian hexahedral grids were created (**Figure 5-3**). In the first box, each cell had  $\Delta x = \Delta y = \Delta z = 3.81$  mm. In the second box, we had  $\Delta x = \Delta y = \Delta z = 1.61$  mm. In the third and fourth boxes, each cell had  $\Delta x = \Delta y = \Delta z = 3.64$  mm. The total number of cells were 4,608,868. When the simulation started, the FAVOR created obstacles (walls) and left only the flow domain to be discrete. In each mesh cell, all scalar value of fluid properties including pressure, fluid fraction, volume fraction, density, and turbulence quantity were assigned at the cell center, while velocity components and fractional area were placed at the center of the cells’ faces respective with their directions.

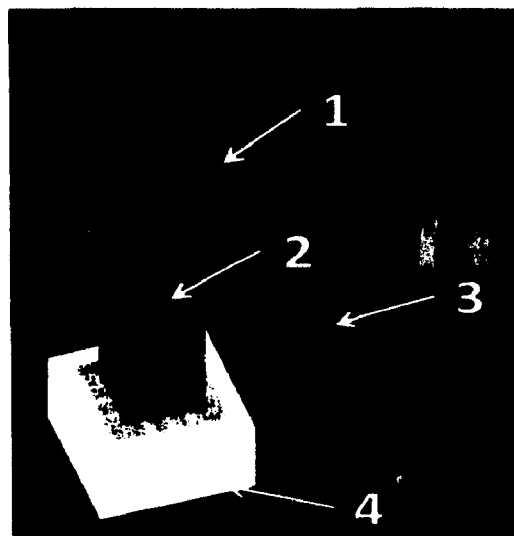


**Figure 5-3:** Mesh of generation in the Flow3D.

Boundary conditions were assigned to the computational domain as shown in **Figure 5-4**. The inlet boundary condition with its constant flow rate of  $0.01 \text{ m}^3/\text{s}$  water (density  $1000 \text{ kg/m}^3$  and dynamics viscosity  $0.001 \text{ Pa.s}$ ) was selected. The atmosphere was assigned with zero gauge pressure. The initial condition for the model had fluid fraction of zero (void space) and each cell was given a uniform zero gauge pressure. The walls were assumed to be made of PVC with a density of  $1350 \text{ kg/m}^3$ . The friction between solid and fluid was assigned using the Wall Function condition with a surface roughness of  $1.5 \times 10^{-6}$ . Outflow condition [52] was assigned at the outlet where the fluid fraction left the boundary.

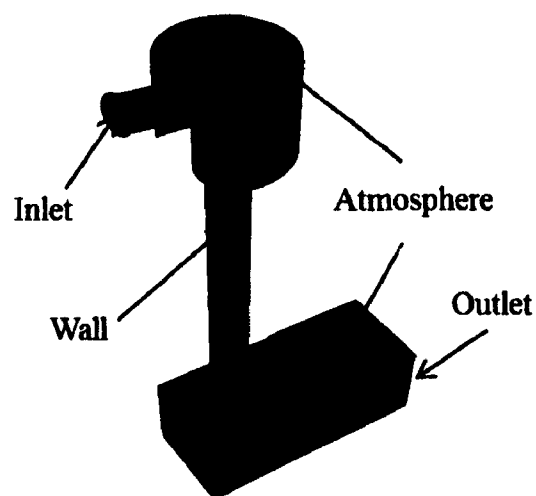


**Figure 5-4:** Diagram of boundary conditions.

GMRES algorithm [56], which is a pressure-velocity coupling solving technique, was used to advance the calculation for each time increment. The iterative GMRES solver was chosen for accuracy, convergence, and speed over other solvers like SOR and SADI, but it uses more computer resources [52]. The time-step in the Flow3D is



automatically set to satisfy the Courant stability criteria. The model was run using Dell Precision T3500 workstation with Intel® Xeon® Quad Core with 24 GB RAM.

### 5.1.2 Two-Fluid Model

In the two-fluid model, both water and air flow were simulated using an open source PDE solver called OpenFOAM [57]. In this model, the motion of fluid was calculated using the incompressible Navier-Stokes equation, and the fluid interface was computed using interface-capturing technique [58]. The two-fluid model represents the reality more clearly than the single-fluid model, and requires more computational resources.

The governing equations used in this model were given the continuity and the modified momentum equations [58]:

$$\nabla \cdot \bar{U} = 0, \quad \text{Eq. 5-4}$$

$$\rho \frac{\partial \bar{U}}{\partial t} + \rho \nabla (\bar{U} \bar{U}) = -\nabla p + \rho g + \nabla \cdot (\mu \nabla \bar{U}) + (\nabla \bar{U}) \cdot \nabla \mu - \sigma k \nabla \gamma, \quad \text{Eq. 5-5}$$

where  $t$  is time,  $\bar{U}$  is the velocity field,  $\rho$  is density,  $p$  is pressure,  $g$  is gravity,  $\mu$  is kinematic viscosity,  $\sigma$  is surface tension coefficient,  $k$  is curvature of the interface, and  $\gamma$  is the fluid fraction. Fluid fraction  $\gamma$  gives the mixing ratio between the water and air.

Fluid fraction  $\gamma = 1$  represents water while  $\gamma = 0$  corresponds to air. To account a motion of fluid fraction, the following transport equation has to be satisfied:

$$\frac{\partial \gamma}{\partial t} + (V \cdot \nabla) \gamma = 0. \quad \text{Eq. 5-6}$$

The local density ( $\rho$ ) and viscosity ( $\mu$ ) of the fluid mix is given by the following equations:

$$\rho = \gamma\rho_w + (1 - \gamma)\rho_a, \quad \text{Eq. 5-7}$$

$$\mu = \gamma\mu_w + (1 - \gamma)\mu_a, \quad \text{Eq. 5-8}$$

where the subscript  $w$  and  $a$  refer to water and air, respectively.

The discretization of the domain was created by OpenFOAM utilities blockMesh and snappyHexMesh [57]. The blockMesh utility was used to create rectangular or curvature geometry with hexagonal grid cells. This could be done by defining vertices of geometry connecting lines and grids. Due to the complex geometry of the inlet structure, simple geometry was created first by blockMesh and later snappyHexMesh was needed to refine the mesh. The discretization by blockMesh shows in **Figure 5-1(a)**. The snappyHexMesh utility was used to form the existing grids to the new geometry based on the CAD model. The CAD model of the structure was created by Solidworks and imported to OpenFOAM. The final discretization of the vortex drop structure shows in **Figure 5-5(b)**. Mesh cells were mostly hexahedral and had a total number of 4,855,254. The maximum volume of the cell was 65.00 mm<sup>3</sup> (average cell length of 4.02 mm), and the minimum volume of cell is 3.45 mm<sup>3</sup> (average cell length of 1.51 mm).

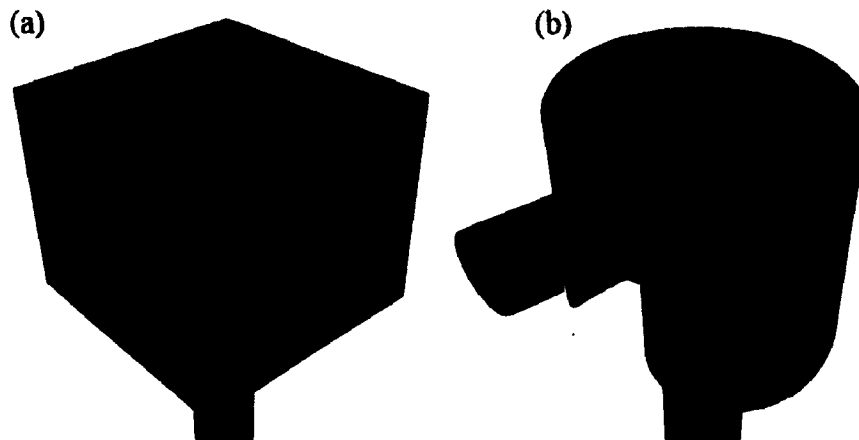


**Figure 5-5:** (a) CAD model of the inlet structure and the discretization by blockMesh. (b) The final discretization of the inlet structure in OpenFOAM.

The boundary condition of two-fluid model was almost identical to the single-fluid model, but the fluid fraction is required for both water and air. The value of one was specified at the inlet boundary condition referring that only water enters and passes through the inlet. The atmosphere boundary condition allows water to pass through the region, so its fluid fraction is given by a zero gradient. The wall boundary condition is also given by a zero gradient of the fluid fraction because the wall can be possibly subjected to water or air. The two-fluid model was simulated using the same workstation as in the single fluid flow model. A solver called an interFoam [57] was utilized to run the simulation.

## 5.2 Numerical Model of Turbine

The turbine was simulated using the single-fluid model in the Flow3D. The general moving objects (GMO) method [59] was used to determine the turbine's motion. The general governing equation of rotational motion of a rigid body at a fixed location is expressed as:

$$\vec{T} = [J] \cdot \frac{d\vec{\omega}}{dt} + \vec{\omega} \times ([J] \cdot \vec{\omega}), \quad \text{Eq. 5-9}$$

where  $\vec{T}$  is the total torque about the fixed location;  $\vec{\omega}$  is the angular velocity of the rigid body; and  $[J]$  is the moment of inertia tensor about the fixed location. The velocity  $\vec{V}$  of any point on the object located at distance  $\vec{r}$  respected to a fixed point is determined by the following equation:

$$\vec{V} = \vec{\omega} \times \vec{r}. \quad \text{Eq. 5-10}$$

Blades were fixed at the central axis of the vertical shaft. Their motions were restricted to one degree of freedom which is allowed to rotate about the central axis. A torque's total external load was assigned to define the blades' motion. When the torque was zero, the blades were free to rotate as if supported by a smooth bearing. Their maximum speed could be calculated at this state. By increasing the torque in the opposite direction of the rotation, the blades were decelerated resulting in lower speed.

A CAD model of a larger scale VDS (Figure 5-6) with its shaft diameter of 15 cm and height of 762 cm was embedded into blocks of mesh cells. Four rectangular blocks were created to cover the entire vortex drop structure parts including the inlet structure (box 1) and the vertical shaft (boxes 2 - 4) (Figure 5-7). Each block was discrete to create smaller cubic mesh cells. The CAD of the blade profile (Figure 3-5(b)) was placed at 564 cm from the shaft's entrance. All the boundary conditions were employed from the

numerical model in stage 1 except that the flow rose to  $0.012 \text{ m}^3/\text{s}$  and the Outflow condition was given at the end of box 4.

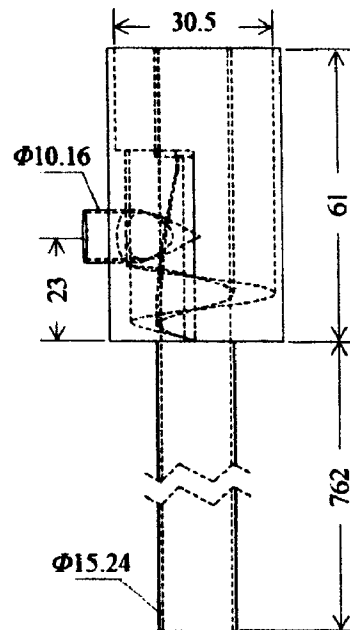


**Figure 5-6:** Dimension (cm) of a larger scale VDS.

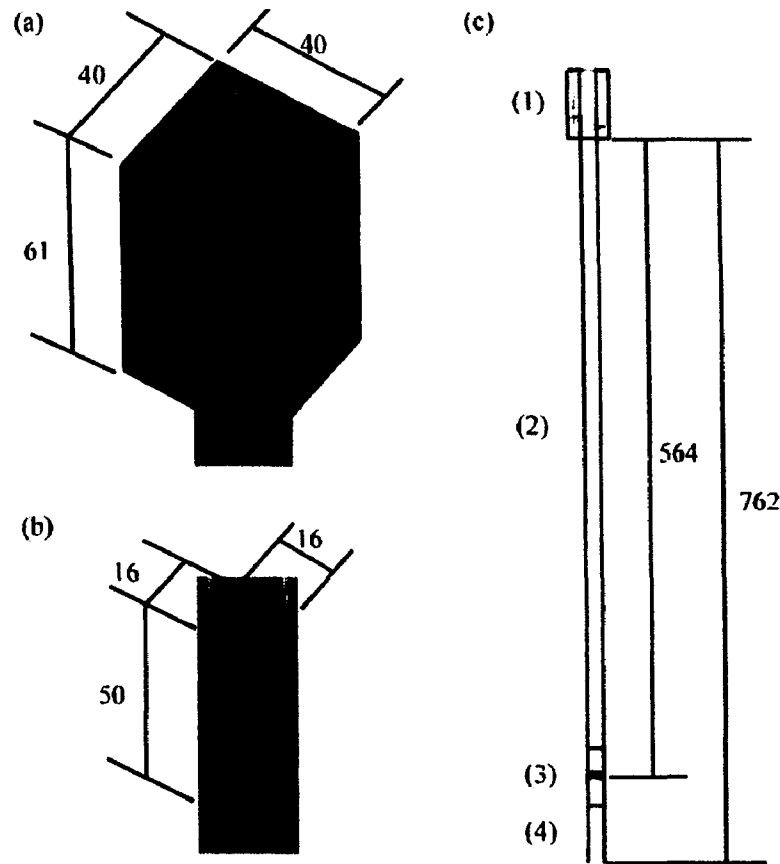


**Figure 5-7:** Up-close picture of mesh cells at (a) inlet structure and (b) turbine section (dimension in cm). (c) Mesh for the entire VDS.

To ensure accuracy of the results, the number of mesh cells were tested and optimized. Different number of mesh cells were tested by running flow simulation passing through a non-loaded blade section. Average rotational speed was captured when the blade section reached steady state (Figure 5-8). Number of cells used started from around 4 million ( $\Delta x = \Delta y = \Delta z = 4$  mm each cell) to about 28 million ( $\Delta x = \Delta y = \Delta z = 2$  mm each cell). The results showed that after about 15 million cells ( $\Delta x = \Delta y = \Delta z = 2.5$  mm each cell) the variation in the results were negligible. To optimize accuracy versus execution, ~15 million cell model was used for the simulation.

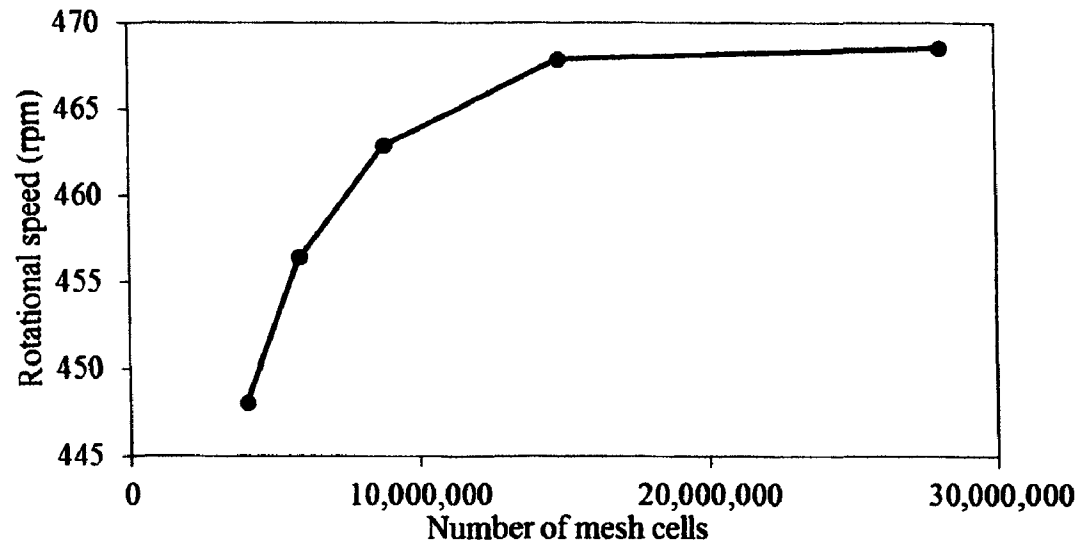


**Figure 5-8:** Rotational speed of free to rotate versus number of cells in the model.

## CHAPTER 6

### EXPERIMENTAL WORK AND COMPARISON OF RESULTS WITH NUMERICAL AND ANALYTICAL SOLUTION

In this chapter, the results from various experiments carried out in this project are presented. Flow through both VDS and the turbine were investigated. Results from analytical solutions, numerical models and experiments are compared. Experiments were carried out in two setups. In the first setup, a small scale commercially available VDS was used to measure just the flow characteristics and in the second setup an outdoor full scale VDS with eVortex retrofitted was used.

#### 6.1 Liquid Flow through VDS

##### 6.1.1 Experimental Setup-1

Experiment to study just the fluid flowing through the VDS was carried out using a small-scale vortex drop structure (mentioned in Chapter 5). The setup was installed indoors at the hydraulic laboratory. Flow of around  $0.01 \text{ m}^3/\text{s}$  (~160 GPM) was continually maintained. The flow rate is significantly lower when compared with a realistic VDS (mentioned in Chapter 1); however, it was chosen due to the limitation of the experiment. The discharged water was recirculated using a water pump. **Figure 6-1** shows the photographs from setup 1.



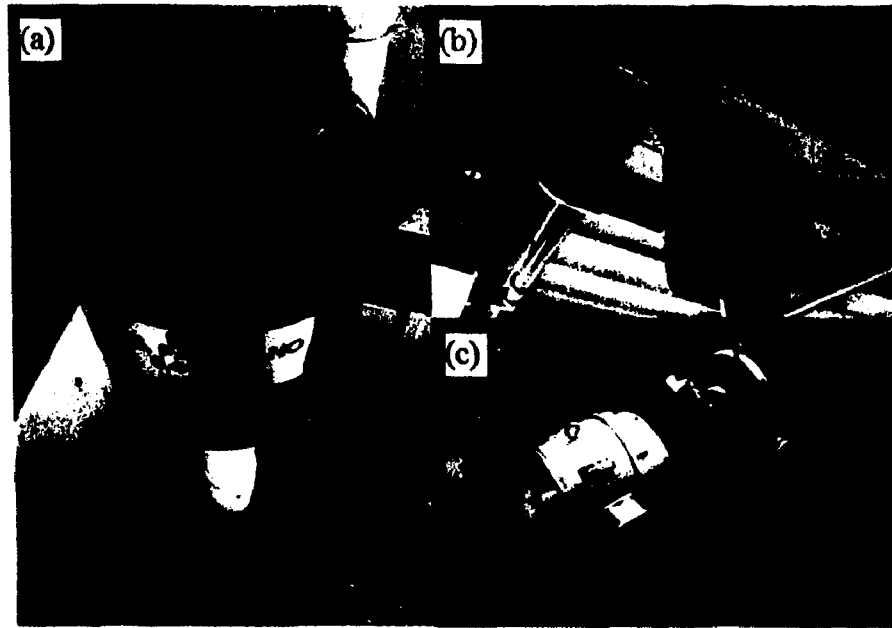


**Figure 6-1:** (a) Top and (b) side views of small scale vortex drop structure used in the experiment. (c) Water pump.

Static pressure was measured along the shaft's wall. A pressure transducer with a capacity (gauge) up to 20.68 kPa (3 psi) was used for the measurement [60]. It was mounted through the shaft's wall allowing water from inside to come in contact with the device (**Figure 6-2(a)**). As the flow pattern was not expected to be symmetric, eight locations were chosen for measurement at each elevation and the average value was calculated (**Figure 6-2(b)**).

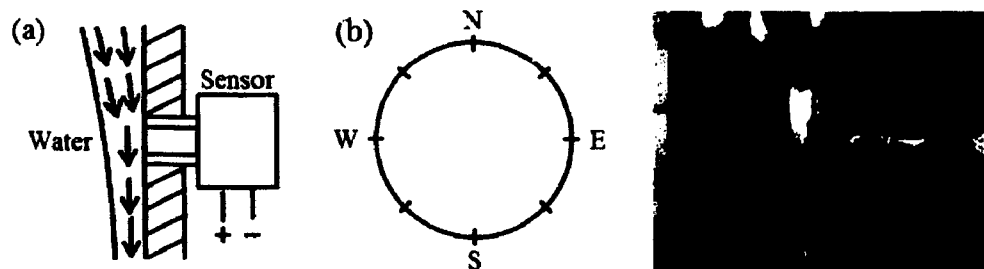


**Figure 6-2:** Diagram of (a) pressure transducer mounting position and (b) its measured location in each elevation. (c) Actual photo of the pressure transducer.

### 6.1.2 Results and Discussion

Measurements were compared against both analytical and numerical results. The numerical models of both single and two fluid models (mentioned in Chapter 5) were computed using similar conditions as the experiment with flow rate of  $0.01 \text{ m}^3/\text{s}$ . Closed-form solution derived by Zhou *et al.* (2006) (described in Chapter 2) was used to predict velocity and pressure. It was applied by giving the initial flow conditions at the shaft's entrance. It needs to be noted that the initial conditions for analytical model was obtained from numerical model.

**Figure 6-3** shows the comparison of fluid fraction observed along the VDS after the flow reached steady state. The liquid regions from both models show similar patterns occupying a thin layer close to the wall leaving air space at the center empty.

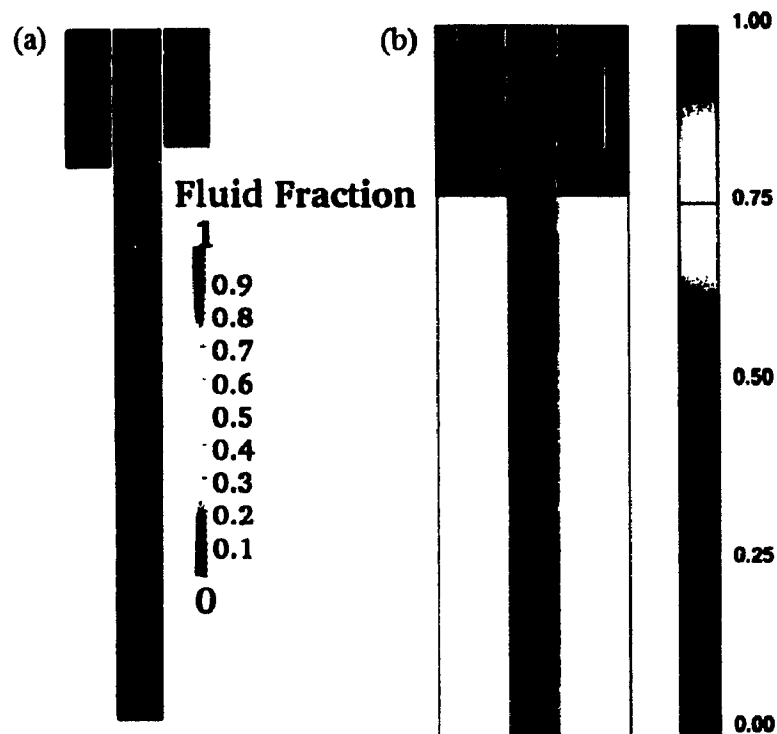


**Figure 6-3:** Contour of fluid fraction along the VDS from (a) two-fluid and (b) single fluid models.

Average static pressure at the wall for a particular cross-section was chosen for comparison. Analytical solutions were obtained by solving Eq. 2-8 and Eq. 2-9 using numerical method with initial conditions (at shaft's entrance) obtained from numerical data. After knowing circulation ( $\Omega$ ) and relative thickness ( $t$ ), the static pressure at the wall ( $r = R$ ) was obtained by Eq. 2-6. Figure 6-4 shows the comparison of average static pressure along the shaft using numerical, analytical and experimental measurements. The experimental result shows that it diverse from analytical solution, which might happen because of the active centrifugal forces due to the higher tangential velocity. Similar behavior was also reported by Zhao *et al.* 2006 [44]. As seen in Figure 6-4, the predictions by numerical models show good agreement with both experimental and analytical solutions.

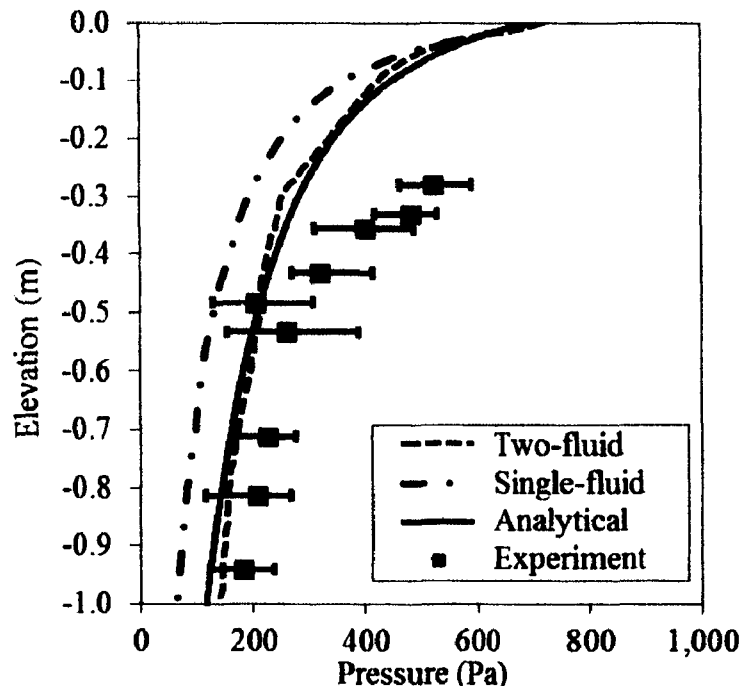


**Figure 6-4:** Comparison of average wall pressure along the elevation from analytical, experimental and numerical (single-fluid and two-fluid) methods.

Average water velocity from the numerical model was compared with the analytical solution. As velocity components from the simulations were solved and specified in Cartesian coordinate system ( $x, y, z$ ) in each mesh cell, they were converted into a cylindrical coordinate system and their average values for tangential and axial velocity components were obtained (Eq. 2-12 and Eq. 2-13). Figure 6-5 shows the comparison of average velocity of water along the shaft from numerical and analytical solutions. The numerical results show good agreement with the corresponding analytical solution.

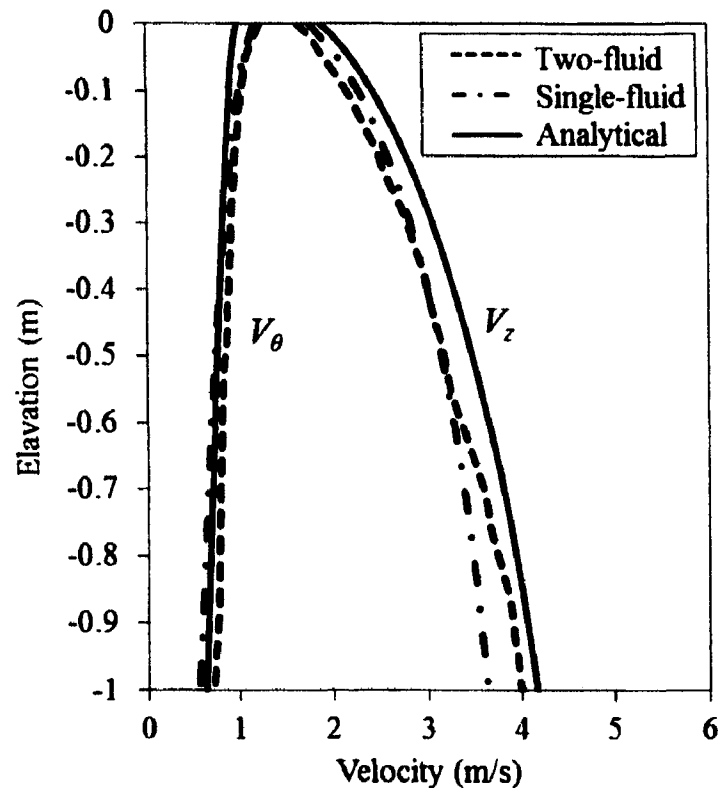


**Figure 6-5:** Comparison of average tangential ( $V_\theta$ ) and axial ( $V_z$ ) velocity along the elevation.

Cross-section at 0.5 m below the entrance was selected for comparison. At the cross-section, water flow maintained a wall-hugging pattern before going into a free-fall.

**Figure 6-6** shows the distribution of pressure across the selected cross-section. As seen in **Figure 6-6**, pressure is asymmetrical with respect to the vertical axis. The models show good agreement in terms of both magnitude of pressure and water-air region within the given cross-section.

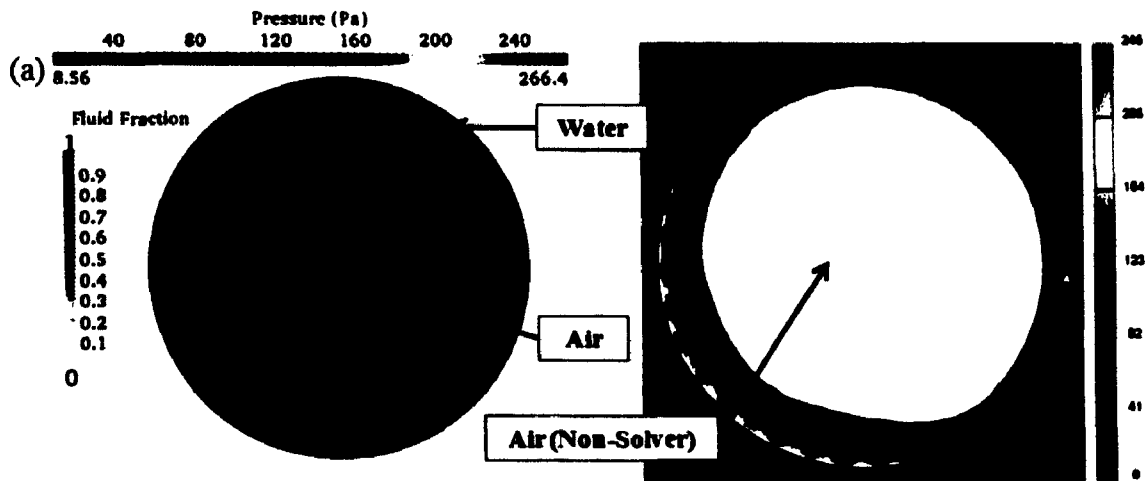


**Figure 6-6:** The cross-sectional pressure distribution of (a) two-fluid and (b) single-fluid model at the elevation of 0.5 m below the shaft entrance.

As the water layer's thickness obtained numerically varies along the circumference, comparison of pressure was carried across the thickest and the thinnest liquid regions. **Figure 6-7** shows the comparison of pressure in radial direction using numerical and analytical solutions. As seen in **Figure 6-7**, results from both numerical models show good agreement. It has to be noted that the analytical solution was based on the assumption that the flow is symmetric and has a constant thickness [44]. As a result, analytical curve is situated between the curves corresponding to the thicker and thinner liquid regions obtained numerically.

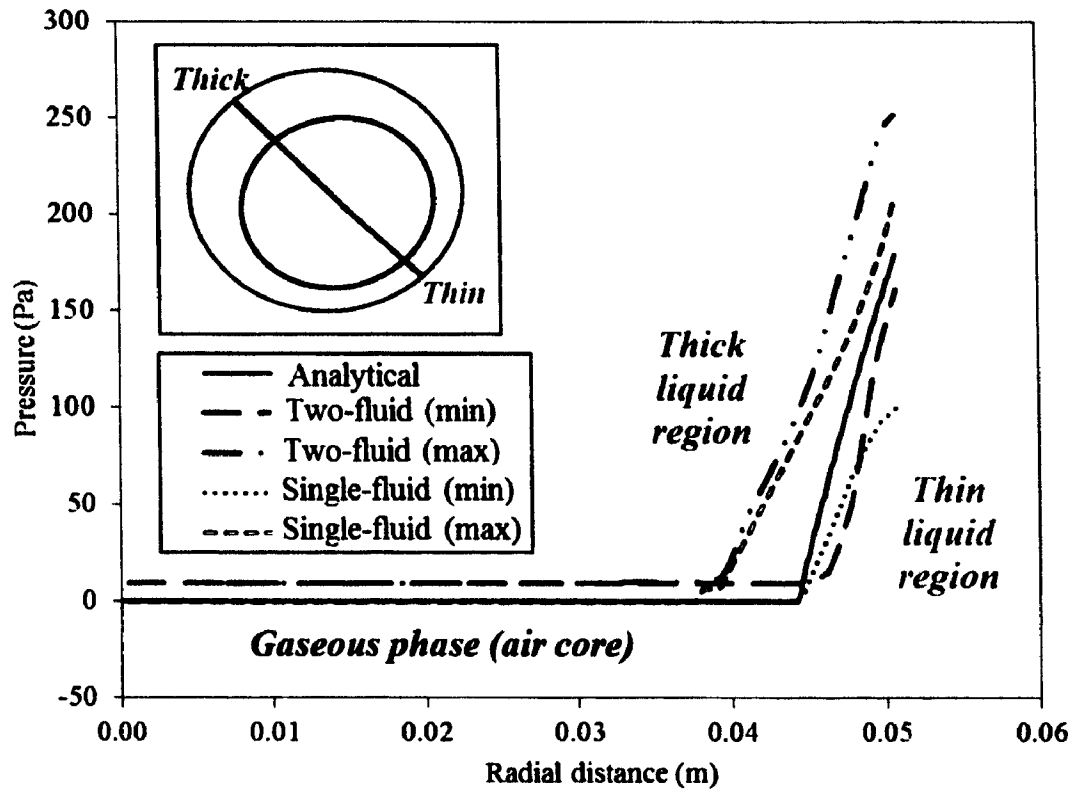


**Figure 6-7:** Comparison of pressure along radial axis at cross-section of 0.5 m below the shaft entrance between analytical and numerical results.

## 6.2 Turbine Performance

### 6.2.1 Experimental Setup-2

A physical model of eVortex turbine was fabricated and installed into a large scale VDS at Trenchless Technology Center (TTC). A commercial VDS consisted of a spiral-type inlet structure at the top and a vertical drop shaft diameter of 15.24 cm (6 inches) and a height of 7.62 m (25 ft.) was employed (**Figure 6-8(a)**) [9]. Instead of installing it underground, it was constructed above ground for access. It could handle a flow up to 400 GPM ( $0.025 \text{ m}^3/\text{s}$ ). However, during the experiment flow rate of up to 190 GPM ( $0.012 \text{ m}^3/\text{s}$ ) was maintained due a water pump used. The pump (6.5 HP) pulled water from a pool and fed continuously to the VDS. The flow rate was controlled and

monitored using a paddlewheel type flow sensor [61] installed at upstream. **Figure 6-8(b)** shows the diagram of the experimental setup.

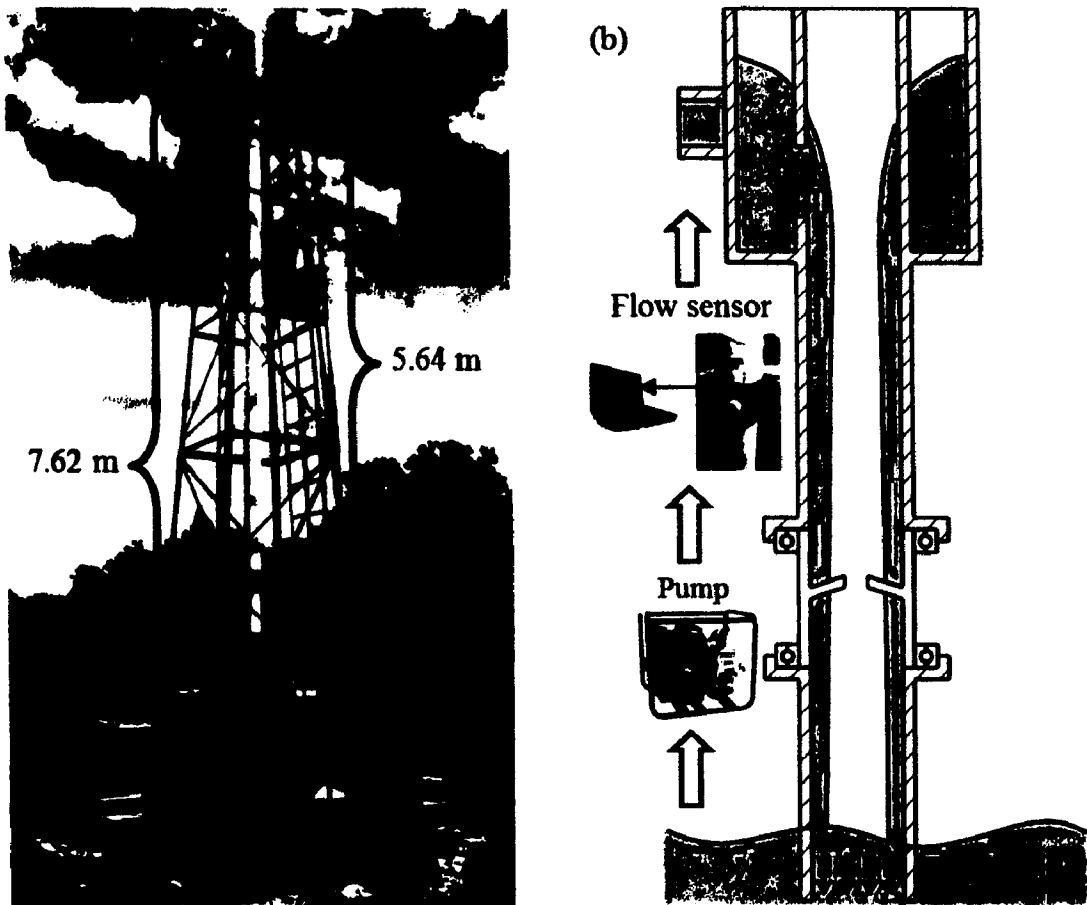


**Figure 6.8:** (a) Large scale VDS constructed at Trenchless Technology Center (TTC). (b) Diagram of water flow in the VDS.

The turbine was fabricated and inserted into the drop shaft at 5.64 m (18.5 ft.) below the entrance (**Figure 6-8(a)**). It consists of rotor and its support structure (**Figure 6-9**). The support structure was fabricated with steel. Its inner diameter was about 15.24 cm (~6 inches) to fit inside the VDS. Four helical plastic blades were machined using geometrical dimensions mentioned in **Table 3-1** and attached to the inner wall. The rotor was connected to stationary supports at both ends via steel radial ball bearings. The

structural supports at both ends were constructed of steel and was designed to be connected with the VDS shaft via pipe flange. This design provided a flexibility to stick the turbine at a location along the VDS. The space outside the rotor was reserved for a generator. **Figure 6-9** shows the diagram of eVortex assembly and the actual fabricated turbine. Lubricant was applied to the bearings to allow smooth operation.

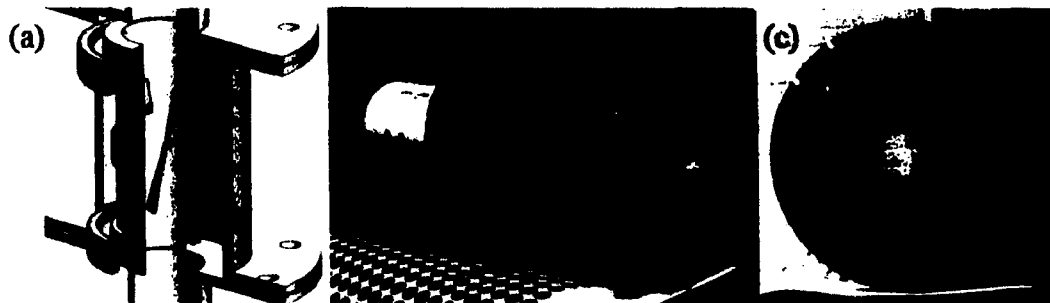


**Figure 6-9:** (a) The diagram of eVortex turbine. (b) Side view and (c) top view of the actual eVortex turbine.

The experiments were carried out in two phases. In the first phase, the maximum speed and static torque from a given flow rate was measured. In the later phase, external loads were applied to the turbine and the dynamic torque was measured.

### 6.2.2 Measurement of Static Torque

In the first phase, experiments to determine the relationship between flow rates and static torque were measured. Static torque occurs when the turbine is subjected to a minimum external load or brake such that it is restricted to move. To measure such torque, a load cell was attached to one of its side (at radius  $R_p$ ) while another side was connected to a stationary support (**Figure 6-10**). This sensor allowed to measure tensile force up to 44.5 N (10 lbf) [62]. The pulling load ( $F$ ) was measured through the load cell and later used to calculate the torque. The torque ( $\tau_{max}$ ) was calculated using **Eq. 6-1**. In



this experiment, the torques were measured while the turbine operated at different given flow rates.

$$\tau_{max} = R_p F + \tau_f, \quad \text{Eq. 6-1}$$

where  $\tau_f$  is the frictional torque from the ball bearing and  $R_p$  is the radius where the load cell was attached. The frictional torque ( $\tau_f$ ) was measured separately using the same load cell pulling the rotor when there was no fluid flow and its value was estimated to be about 0.6 Nm.

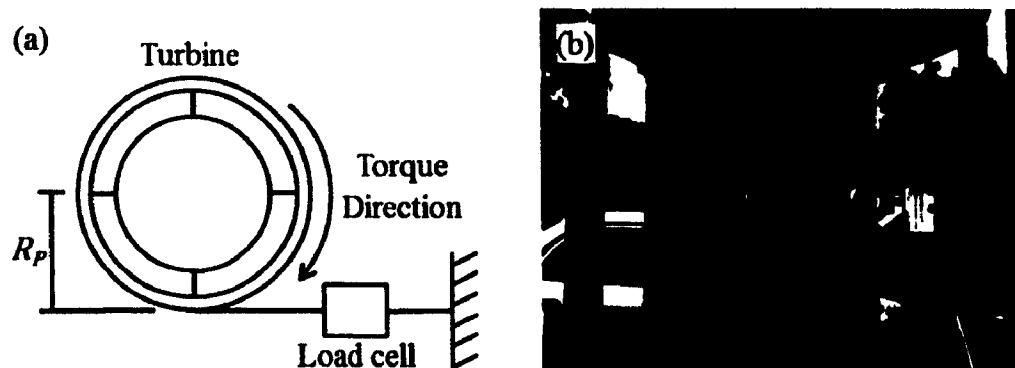


**Figure 6-10:** (a) Diagram and (b) actual installation of the load cell to measure the static torque.

An optical tachometer [63] and a reflective marking tape were used to capture speed at various flow rates. The marking tape was glued to the turbine rotor.

### 6.2.3 Measurement of Dynamic Torque

In this experiment dynamic, torque of the turbine was measured while it was operated at maximum flowrate (190 GPM). The rotational velocity of the turbine was measured at the corresponding torque.

A two-pulley bond transmission system was constructed to apply an external load to the turbine (**Figure 6-11(a)**). The bigger pulley was attached to the turbine while the

smaller pulley was attached to a magnetic particle brake. Both pulleys were connected using an adjustable v-belt. The magnetic particle brake [64] converts an input voltage into a brake torque up to 1.7 Nm (15 lb.in.).

The external torque load is the summation of applied load by the brake, and the mechanical losses (frictional loss from bearings). Typically, it is difficult to determine each loss individually, so calibration is needed to determine the torque for the entire system. Calibration was done by using the load cell by pulling the turbine with specific speeds and modify the input voltages from the brake (**Figure 6-11(b)**). While pulling the load cell with various speeds showed force to be slightly different. Results from the calibration were used as references when testing the turbine. **Figure 6-12** shows the results from calibration.

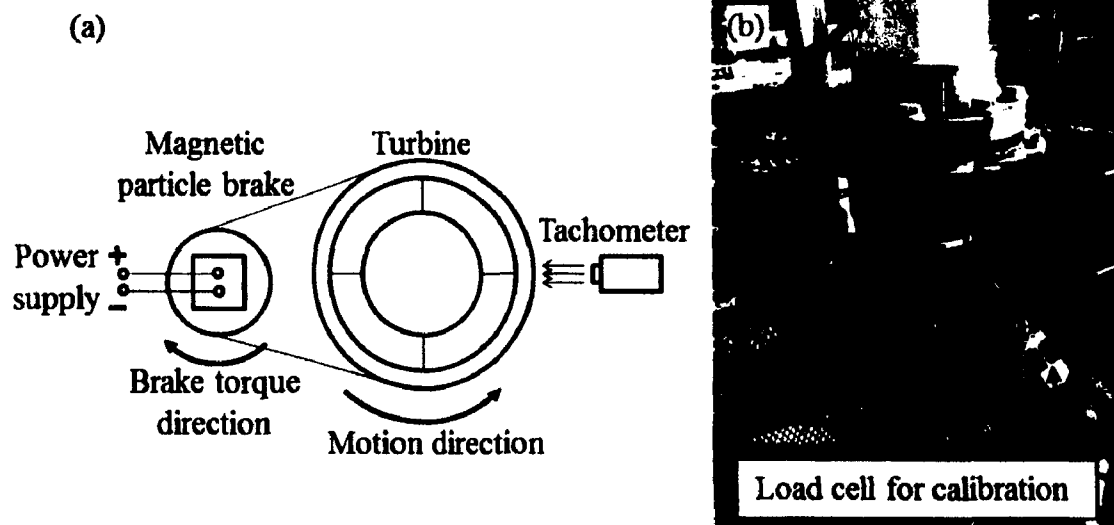


**Figure 6-11:** (a) Diagram of the two pulleys transmission power system for measuring dynamic torque and speed. (b) Actual turbine with transmission during the calibration.

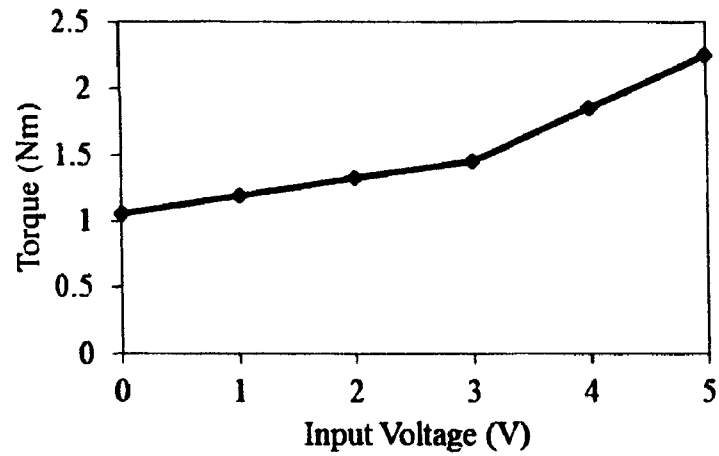


**Figure 6-12:** Calibration between input voltage of the magnetic brake and the calculated torque.

#### 6.2.4 Results and Discussion

Measured data was compared against the numerical data. **Figure 6-13** shows a snap shot from numerical model with turbine installed.

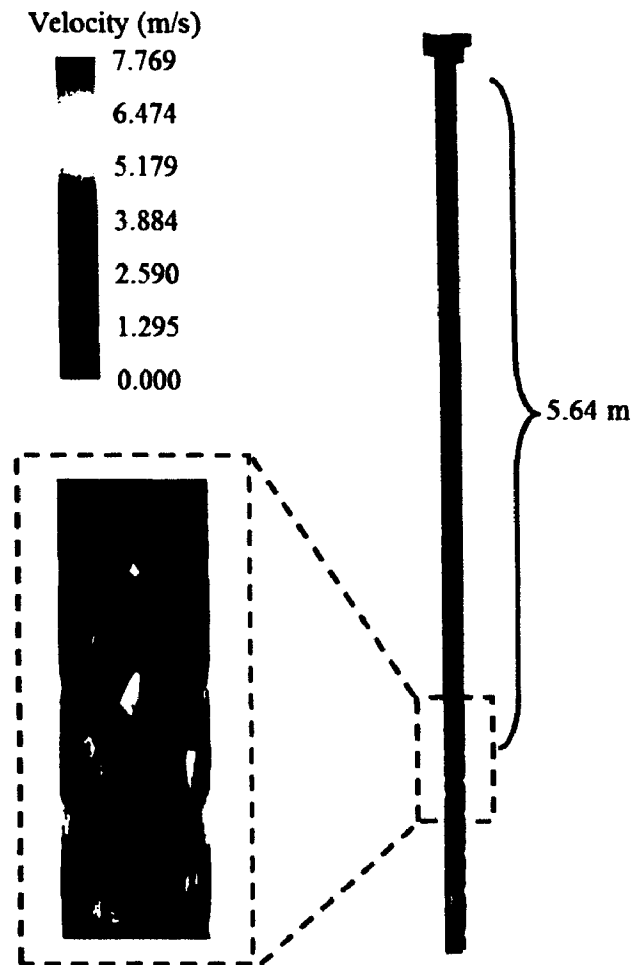


**Figure 6-13:** Velocity of water through VDS with turbine located at 5.64 m below the entrance.

During simulation, the rotational speed consisted of unsteady and steady state regions for a given time period. **Figure 6-14** shows an example of numerical speed from start till it reaches the steady state. In the unsteady region, a turbine is accelerated by incoming fluid resulting in the raise of its speed within a short time period. After passing the unsteady region, the turbine reaches a steady state where its speed is almost constant. Torque versus speed were calculated using the average of 50 readings in steady state.

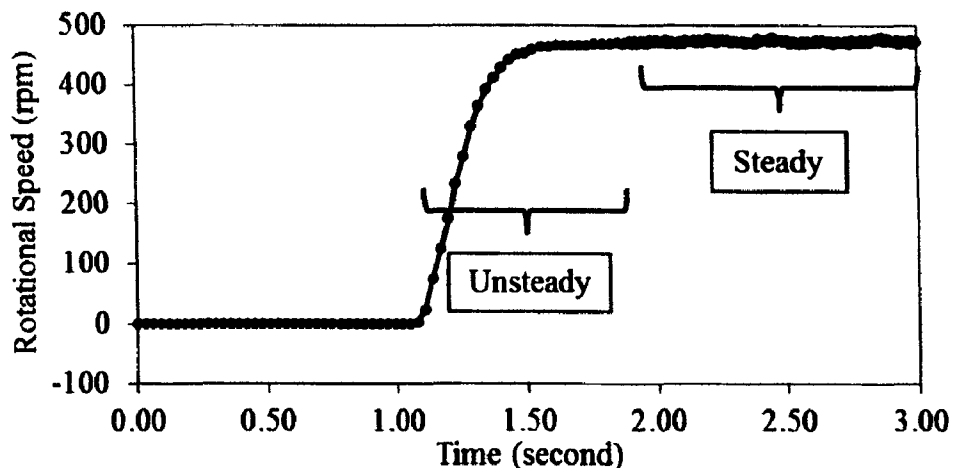


**Figure 6-14:** Numerical result of rotational speed from starting to steady state.

The various counter torque were applied in the numerical model to obtain the corresponding speed. A small torque load was initially assigned in the direction opposite of the motion, and its value was incrementally raised till the turbine almost stop. **Figure 6-15** shows pictures of the flow through the eVortex. Each picture (a-e) shows the flow pattern with different constant torques. As seen in **Figure 6-15**, the flow pattern is changed significantly when increasing the torque. When the torque is zero, the fluid occupies the periphery (**Figure 6-15(a)**). As the flow slightly changes its shape after flowing out of the turbine, this determines that less energy was transferred to the turbine. With increasing levels of the counter torque, the air flow portions is blocked due to the stagnation of the liquid built up. However, at much higher torque levels, the air passage opens up. Further study is required to investigate this phenomenon. Although the flow profile changed for various speeds, the empty space remained open for the air to pass through.

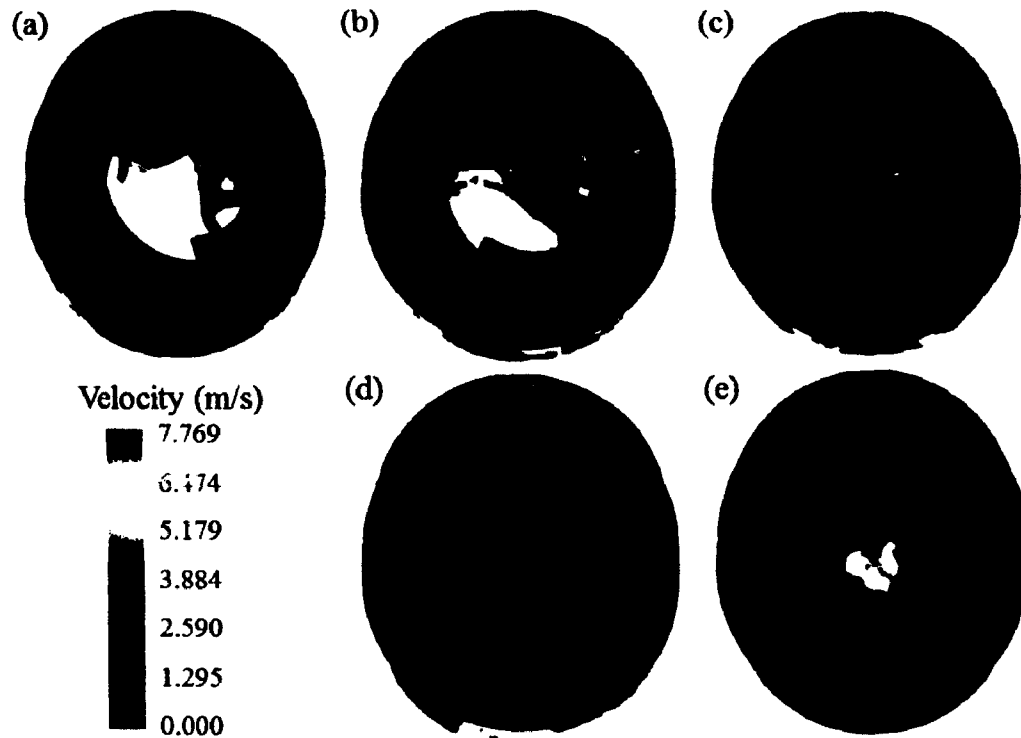


**Figure 6-15:** Snapshots from simulations showing velocity of flow for various torque applied ((a) 0 Nm, (b) 0.5 Nm, (c) 1 Nm, (d) 1.5 Nm, and (e) 2 Nm). The corresponding speeds were (a) 465.53 rpm, (b) 348.17 rpm, (c) 241.02 rpm, (d) 153.01 rpm, and (e) 60.75 rpm.

The power and efficiency were calculated. **Figure 6-16** shows the relationship between turbine output torques and rotational speeds which were carried from the numerical results in **Figure 6-15**. The output power ( $P$ ) was also calculated by **Eq. 6-2**. Later, the output power was estimated using polynomial regression to cover the entire range of the speed. Based on the estimated power, the optimal power could be identified.

$$P = \tau\omega, \quad \text{Eq. 6-2}$$

where  $\tau$  is the torque and  $\omega$  is the rotational speed. The numerical results (**Figure 6-16**) show that the highest power of 25.76 Watts occurred at the turbine's speed around 217 rpm. Although the power predicted from this VDS was low and might not be useful in

practice, with higher flow rates in a bigger VDS, the total power output would be significant and be considered for power harvesting purposes.

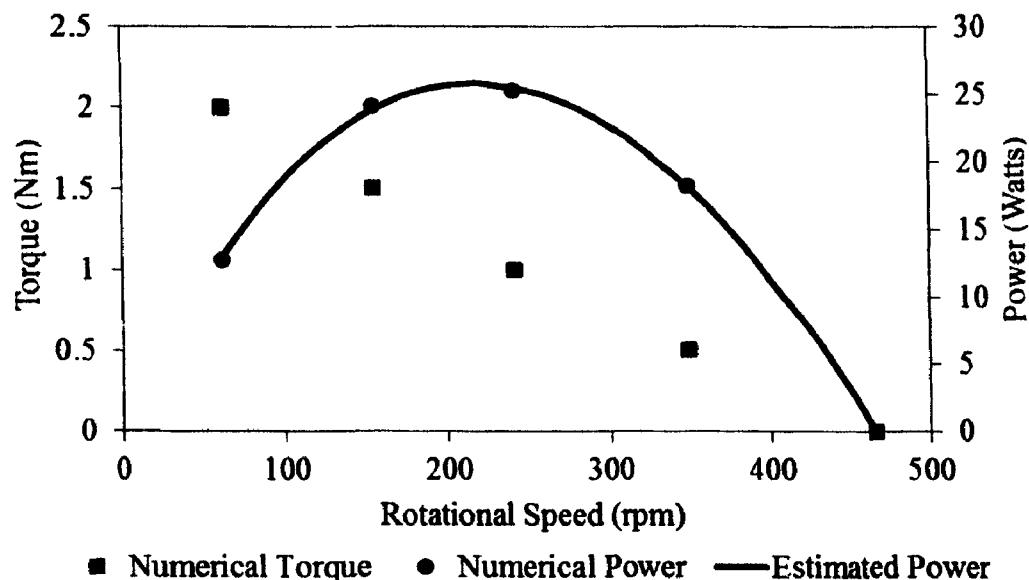


**Figure 6-16:** The torque and power generated for 190 GPM using numerical model.

The efficiency ( $\eta$ ) of the turbine was also estimated using Eq. 6-3:

$$\eta = \frac{P}{P_a}, \quad \text{Eq. 6-3}$$

where  $P_a$  is the available power at the turbine's location. The available power in the flow was estimated from the energy head. Fluid head ( $E$ ) at each cross-section was calculated from the analytical model (Eq. 2-14) and available power is given as:

$$P_a = \rho g Q E, \quad \text{Eq. 6-4}$$

where  $\rho$  is the density of water,  $g$  is the gravitational acceleration, and  $Q$  is the volume of the flow rate. **Figure 6-17** shows the projected values of power for given elevation and flow rate (100-400 GPM). As seen from **Figure 6-17**, the higher the flow rate the higher the power available. When the fluid flows through a vertical shaft, it is accelerated by gravity resulting in higher kinetic energy. However, for increasing velocity, losses due to

friction between the fluid flow and the wall also increased. This causes deceleration. As a result, the forces due to gravity and friction are balanced leaving fluid flowing with almost constant velocity. This explains why the available power in **Figure 6-17** is almost constant at deeper elevations.

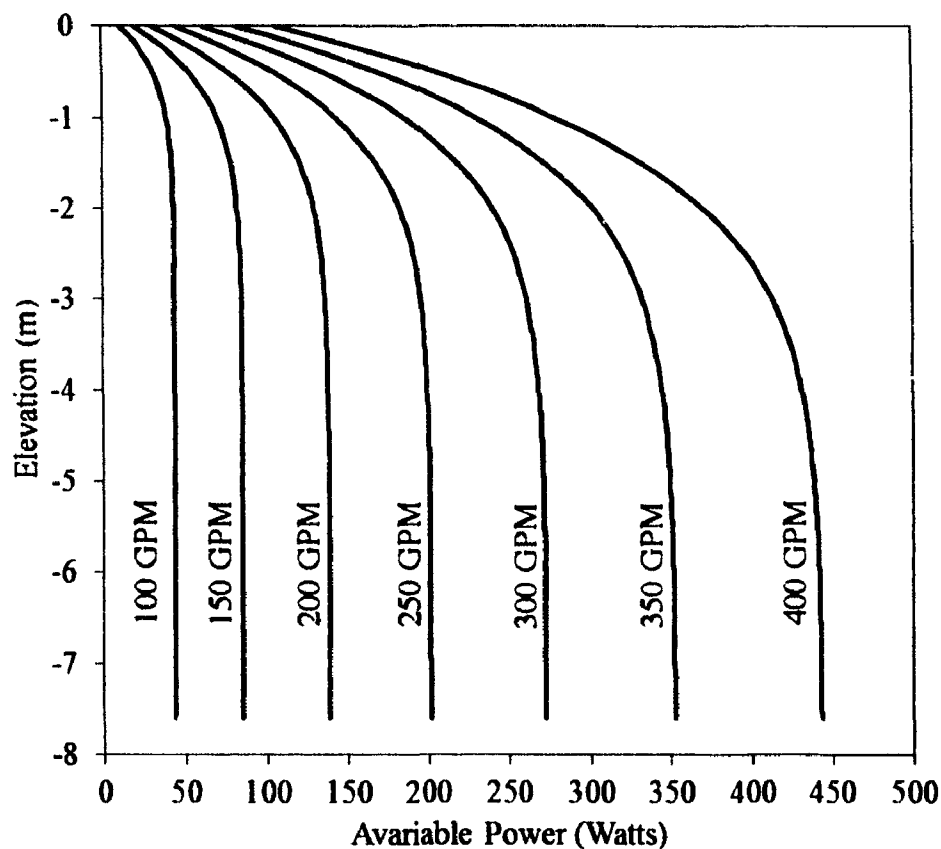


**Figure 6-17:** Power available for elevations and flow rate.

The available fluid power was estimated at given flow rate of 190 GPM and at an elevation of 5.64 m (18.5 ft), and its value was 127.57 Watts. Therefore, the highest efficiency of the eVortex turbine at this location was 20.19 %. This predicted efficiency is close to the efficiency of typical microturbines (20–30 % efficiency LHV) [65]. To improve the efficiency of the eVortex design, optimization would come into



consideration. Parametric study by varying blade properties to improve the performance will be discussed later.

Next, the experimental results are presented. In the first experiment, the turbine was operated without an external load except friction loss due to the bearings. The torque load due to the bearing was measured separately without water flow operated. The dynamic frictional torque of around 0.5 Nm was measured and calculated using the load cell. This value was in good agreement with an estimated frictional moment by using the bearing friction coefficient formulation and its configuration [66].

Results of rotational speed at different flow rates are shown in **Figure 6-18**. At the flow rate of 190 GPM, the speed reaches about 250 rpm during the experiment. The speed varied linearly versus the flow rate. The experimental speed when compared with the analytical and numerical results was slightly lower.

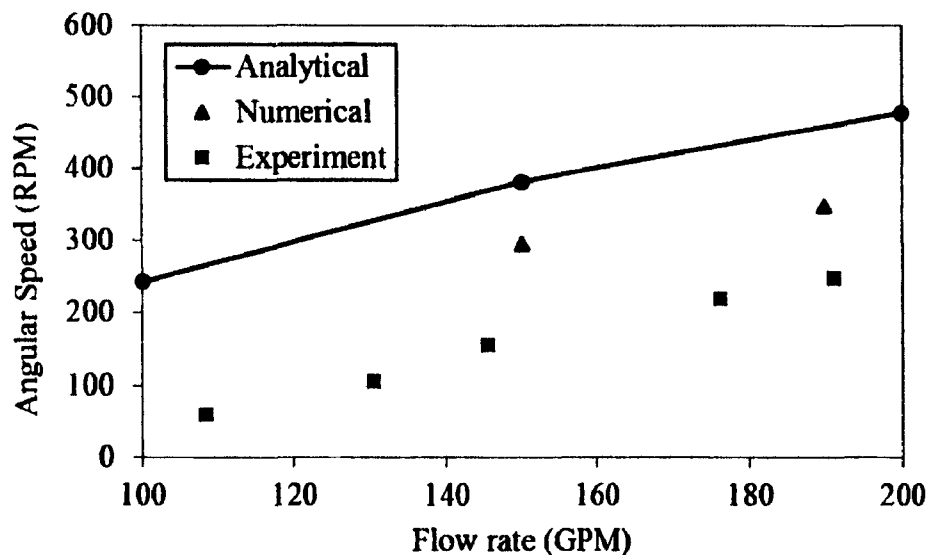


**Figure 6-18:** Diagram between turbine speeds and flow rates from analytical, numerical and experimental results.

**Figure 6-19** shows the static torque from the analytical and the experiment for various flow rates. As seen from the diagram, the static torque increased linearly with the flow rate. At a flow rate capacity of 190 GPM, the static torque from the experiment was around 1.5 Nm and it is lower when compared with the analytical result.

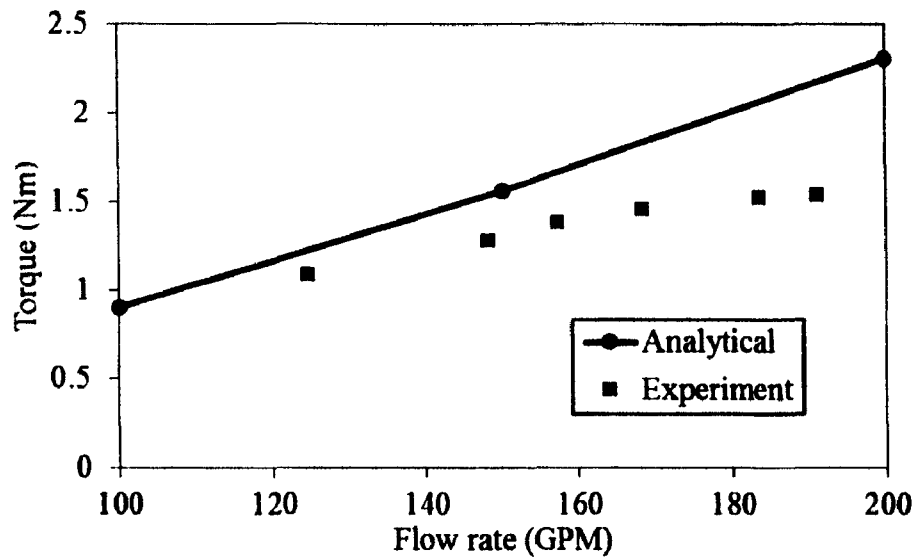


**Figure 6-19:** Static torques versus flow rates obtained from analytical and experimental methods.

The dynamic torques from the analytical, numerical and the experiments are given in **Figure 6-20**. It needs to be noted that the first experiment data at the rotational speed of 0 rpm and 250 rpm are carried from the data at 190 GPM of **Figure 6-18** and **Figure 6-19**, respectively, but chosen to present in **Figure 6-20** for comparison.

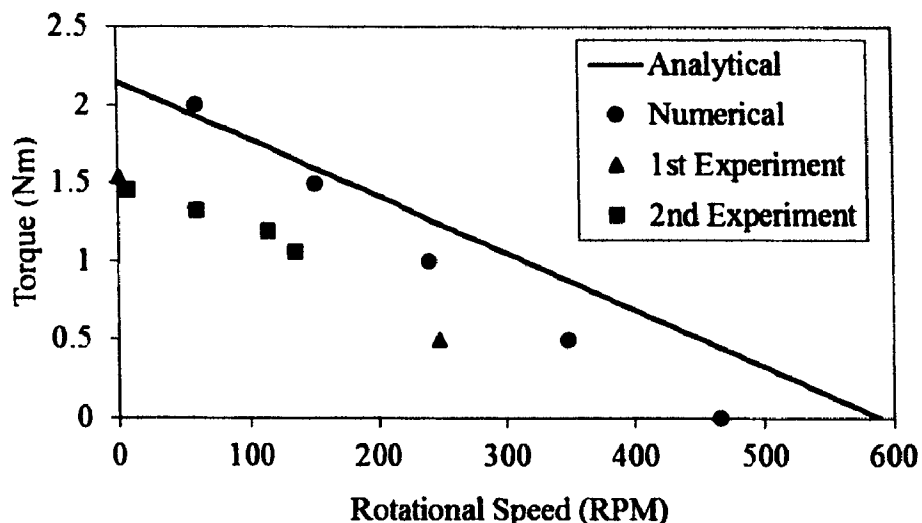


**Figure 6-20:** Comparison of torque-speed from analytical solutions, numerical model and experiments at water flow rate of 190 GPM.

As seen from **Figure 6-20**, the maximum speed (2<sup>nd</sup> experiment) without the load from the brake is close to 137 rpm. It is slightly lower than the speed (1<sup>st</sup> experiment) measured in a free state (250 rpm). This shows that the transmission system introduces losses. The torque supplied by the brake was increased and the corresponding speed was measured till the turbine nearly stopped to estimate the dynamic torque. The lowest speed was captured at around 8 rpm and the dynamic torque loads was closed to 1.45 Nm. This torque is in good agreement with the static torque (0 rpm) which is around 1.5 Nm from the first experiment (**Figure 6-20**). The combined results from the first and second experiments give a clearer picture of torque versus speed for the turbine.

The results from **Figure 6-20** shows that analytical and numerical solutions were in good agreement when compared with the experiment. The results from the experiments had the lowest value of torque followed by the numerical and the analytical outcomes at the same turbine speed. The reason could be explained by the fluid pattern through the turbine. In the analytical model, the fluid velocity components were assumed

to exist in two dimensions including axial and tangential to the rotating axis, while in both the numerical model and the experiments, some of the fluid portions also had their velocity component in radial direction. Therefore, the total average tangential flow velocity component should be higher in the analytical model at the exit of turbine. As the torque was determined by the rate change of angular momentum (product of mass flow rate, velocity and distance from rotating axis) in the tangential direction of the fluid before and after passing through the turbine, the higher of the tangential velocity component from the analytical model yielded higher torque results. Friction also plays a significant role. As in actual and numerical model, their energy losses were accounted for while in the analytical, losses were neglected.

From torque versus speed, the power was calculated (**Figure 6-21**). The experimental results were estimated by regression using 3<sup>rd</sup> order polynomial, and the approximated equation is expressed as:

$$P = 1.552 \times 10^{-1}\omega - 1.891 \times 10^{-4}\omega^2 - 8.995 \times 10^{-7}\omega^3, \quad \text{Eq. 6-5}$$

where  $P$  is the power output (Watts) and  $\omega$  is the rotational speed (rpm). The estimated maximum power based on the experiment is 16.56 Watts at the rotational speed around 179 rpm. The numerical and analytical maximum powers are higher than the experiments at around 55.55 % and 100.03 %, respectively.

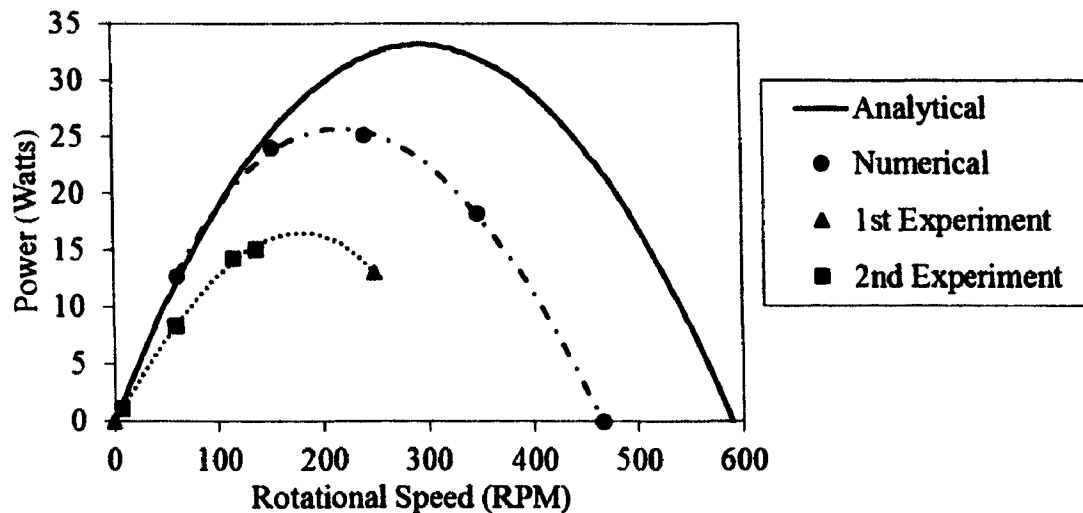


**Figure 6-21:** Comparison of power versus speed from analytical, numerical and experiment for flow rate of 190 GPM.

### 6.3 Parametric Study of Turbine

Parametric study of turbine geometry was investigated using the numerical model.

The aim for this study was to improve the efficiency. Simulations here were carried out for a fixed flow rate of 190 GPM.

#### 6.3.1 Elevation

The eVortex model with the geometry (Table 3-1) was simulated at different elevations including ~1.5 m (5 ft), ~3 m (10 ft), ~4.5 m (15 ft) and ~5.6 m (18.5 m).

**Figure 6-22** shows the relationship between torque and speed for each elevation.

Although there are not much different in rotational speeds in each corresponding torques, it turned out that the highest speed is at elevation 1.524 m. The results from the numerical showed a similar trend when compared with analytical solutions showing in **Figure 6-23**.

However, at location 5.639 m, the analytical showed the lowest speed given the same torque while the numerical showed at location 4.572.

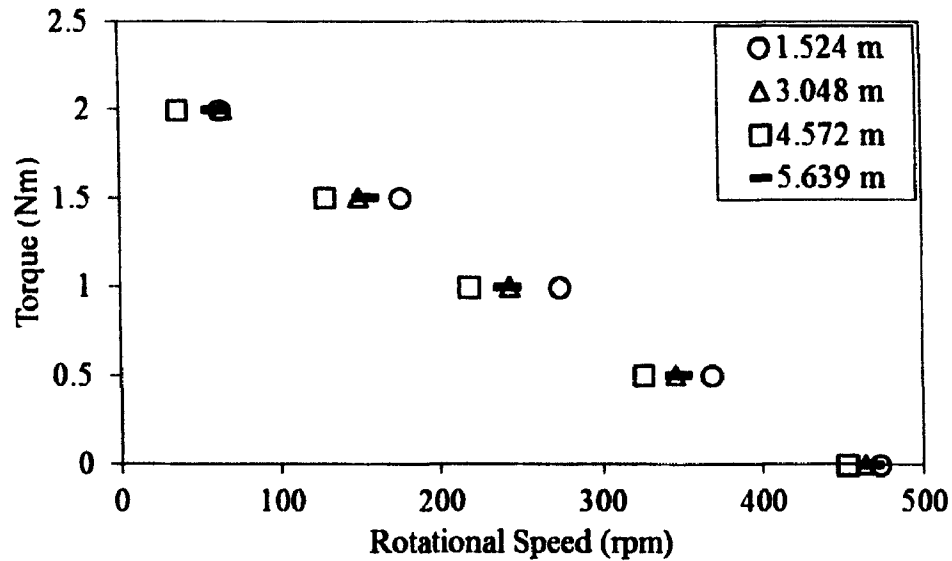


**Figure 6-22:** Numerical torque versus speed at various elevations.

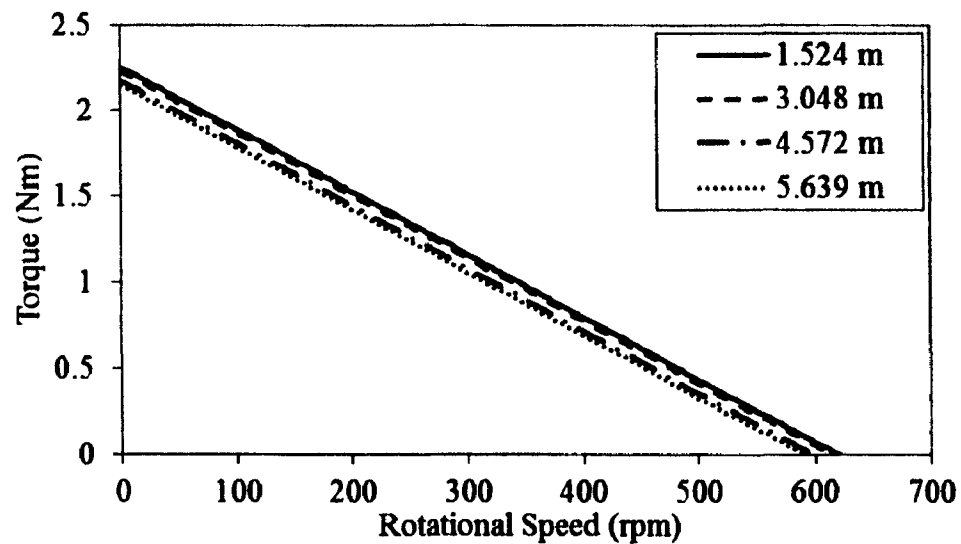


**Figure 6-23:** Analytical torque versus speed at various elevations.

The power predicted from numerical data is shown in **Figure 6-24**. At 1.524 m depth, the highest power generated by the turbine occurred at a speed around 235 rpm and its value was 29.51 Watts. This shows an improvement in terms of highest power from the previous simulation (at 5.639 m) by 14.55 %. It was interesting to see that the power generation was higher when the turbine was near the entrance at the top (1.524 m)

and got lower with increased elevation height (3.048 m and 4.572 m). This result was contrary with a general sense that the lower the level the higher the potential energy from gravity. However, when the location was deeper than a certain height, the power was higher at the deeper level as seen from depths of 4.572 m and 5.639 m.

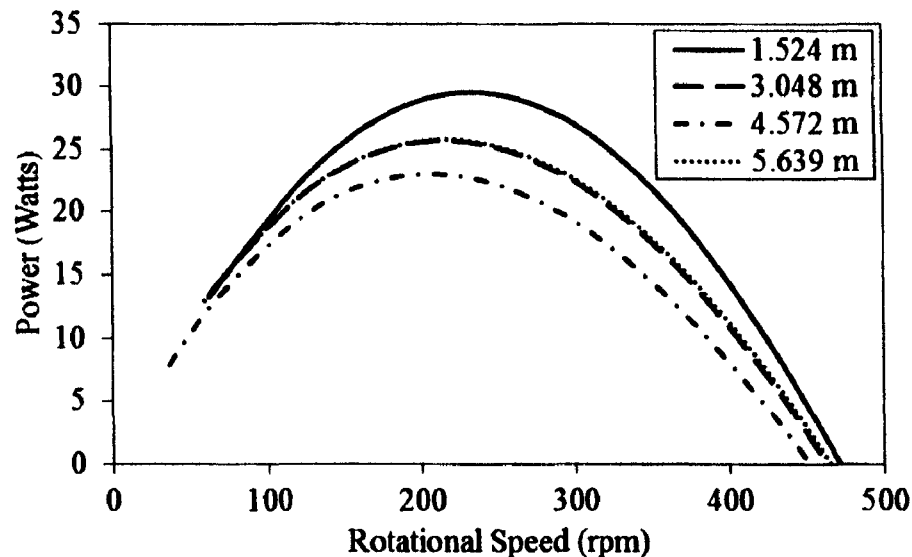


**Figure 6-24:** Power versus speed at various elevations.

Another interesting point was the efficiency (Figure 6-25). When energy available along the elevation was similar to Figure 6-17, the power available at each location was calculated, and the values were 113.00 Watts (at 1.524 m), 125.85 Watts (at 3.048 m), 127.41 Watts (at 4.572 m), and 127.57 Watts (5.639 m). As seen in Figure 6-25, the efficiency improved when the turbine was closer to the entrance around 26.11 % at the elevation 1.524 m, which its value was higher than the previous elevation of 5.639 m (20.19 % eff.) by 29.32 %. As the results showed that power and efficiency increased at elevation 1.524 m.

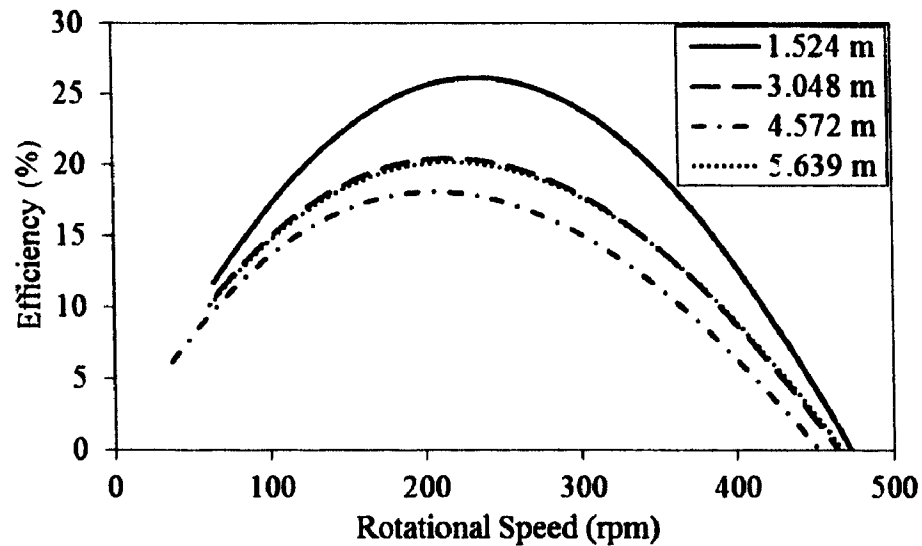


**Figure 6-25:** Efficiency versus speed at various elevations.

### 6.3.2 Optimization of Blade Angle

The angle ( $\alpha$ ) of the blade was varied from 45 degrees to 30 and 60 degrees as shown in **Figure 6-26**. The number of blades ( $N$ ) was four blades and the blade height ( $H$ ) was adjusted following **Eq. 3-5**.

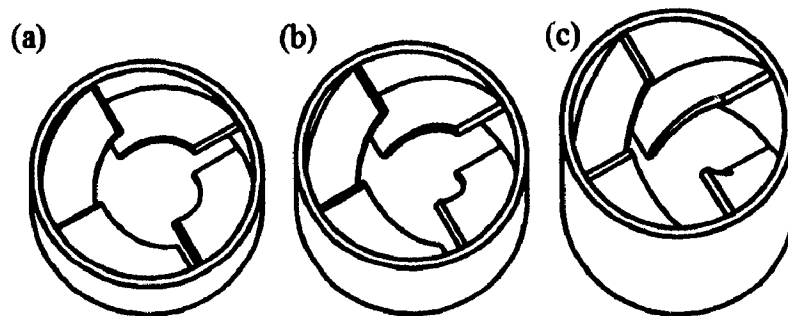


**Figure 6-26:** CAD model of various blade angle ( $\alpha$ ): (a) 30 degrees, (b) 45 degrees, and (c) 60 degrees.

The numerical torque and speed with different blade angles are shown in **Figure 6-27**. When torque is zero, the turbine with the angle of 30 degrees yielded the highest speed, and it is reduced when increasing the blade angle. Although the simulation did not



perform to define the maximum torque when the turbine was at rest (zero rotational speed), it could be seen from the trend of each relationship in **Figure 6-27** that the maximum torque would occur at either 45 or 60 degrees following 30. The results from the numerical solutions showed a similar trend when compared with the analytical solutions shown in **Figure 6-28**.

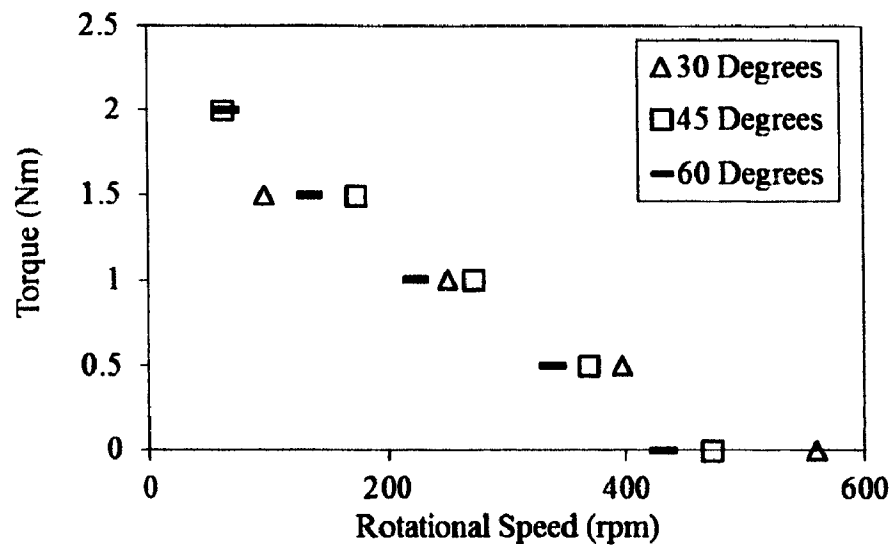


**Figure 6-27:** Numerical torque versus speed at various blade angles ( $\alpha$ ).

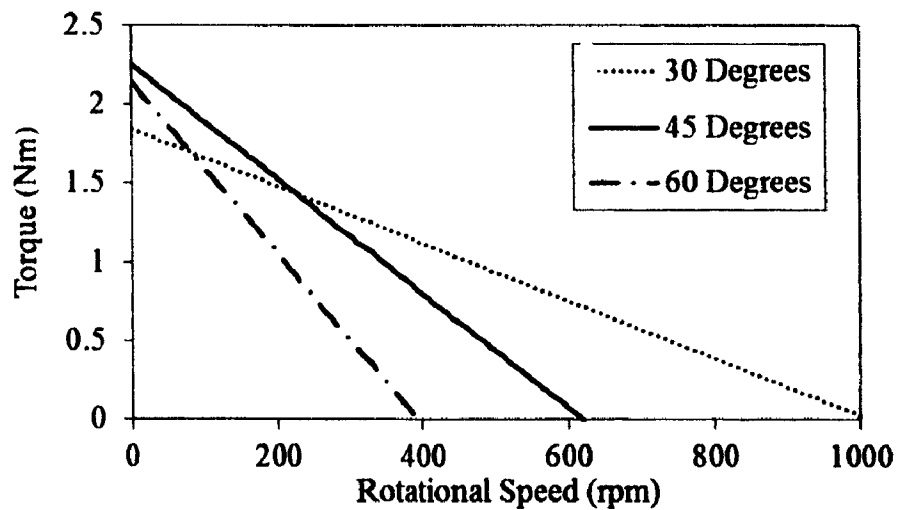


**Figure 6-28:** Analytical torque versus speed at various blade angle ( $\alpha$ ).

The estimated power estimated for blade angle is **Figure 6-29**. Among the design with various blade angles, the turbine with the angle of 45 degrees generated the highest power output followed by 30, 60, and 15. As seen from **Figure 6-29**, the angle has a significant effect on power.

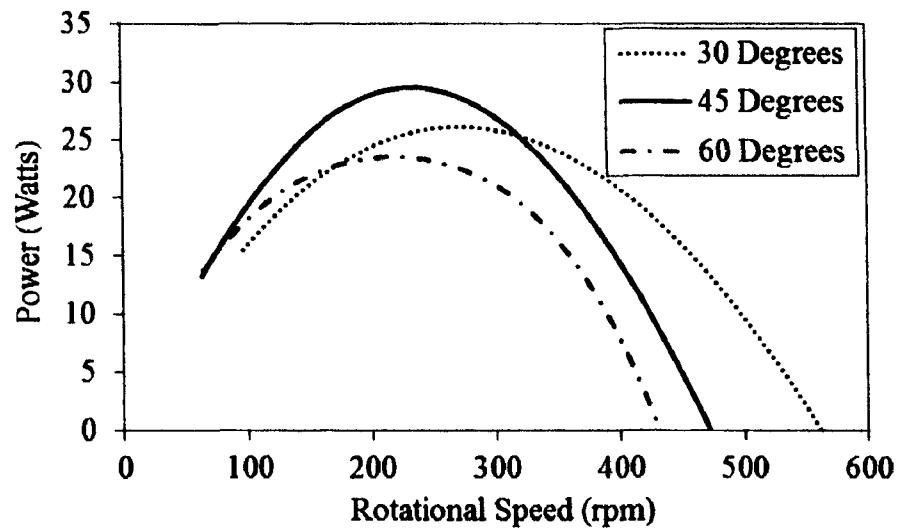


**Figure 6-29:** Power versus speed at various blade angles ( $\alpha$ ).

### 6.3.3 Optimization of Blade Width

In this optimization, the blade area was changed by reducing its width ( $W$ ) from 3.81 cm to 2.54 cm and 1.27 cm (**Figure 6-30**).

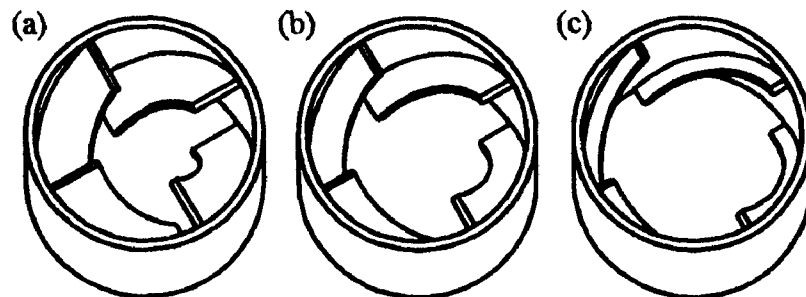


**Figure 6-30:** CAD model of various blade width ( $W$ ): (a) 3.81 cm, (b) 2.54 cm, and (c) 1.27 cm.

Numerical results of the flow without turbine through VDS showed that the thickness of water was ranging around 0.5-0.6 cm at the location. Therefore, various widths (Figure 6-30) were guaranteed to be hit by the entire incoming fluid.

Numerical results of the torque versus the speed of various blade widths were shown in Figure 6-31. Given the same torque to each blade width, results showed a significant drop in speed at the blade width of 1.27 cm, while the other two models showed close results.

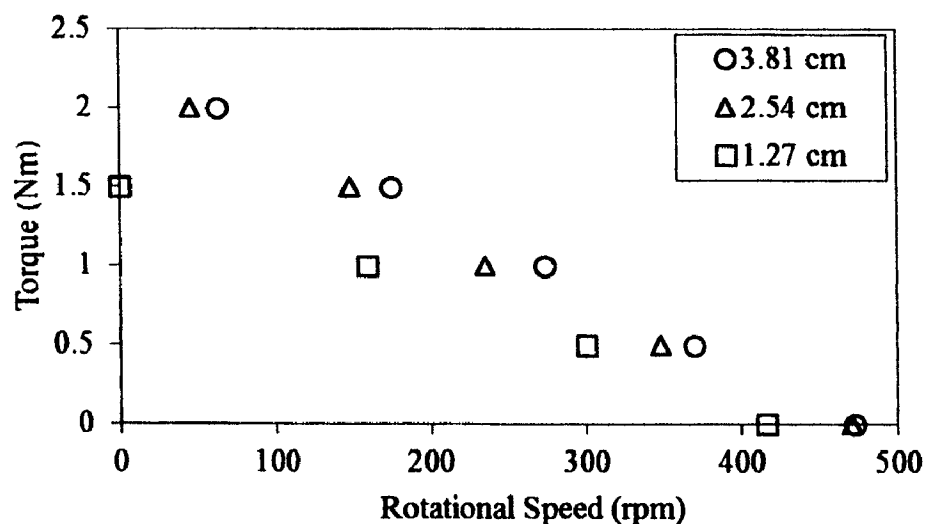
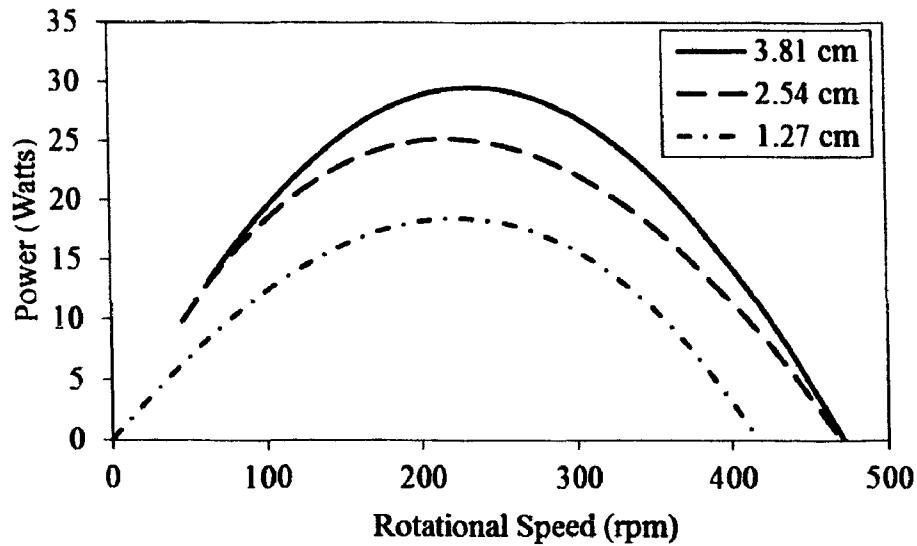


Figure 6-31: Numerical torque and speed at various blade widths ( $W$ ).

These results were used to predict the output power (Figure 6-32). As seen from Figure 6-32, the highest power occurs at a blade width of 3.81 cm. Reducing the width from 3.81 to 1.27 cm results in the highest power reduced by around 37.5 %, which considerably worsen than the original width design.



**Figure 6-32:** Power and rotational speeds at various blade widths ( $W$ ).

#### 6.3.4 Optimization of Blade Numbers

By specifying blade height ( $H$ ), blade angle ( $\alpha$ ) and pipe radius ( $R$ ) from **Table 3-1** into **Eq. 3-5**, the calculation showed that at least four blades or higher were resulted. The number of blades ( $N$ ) ranging from three to six were chosen (**Figure 6-33**).

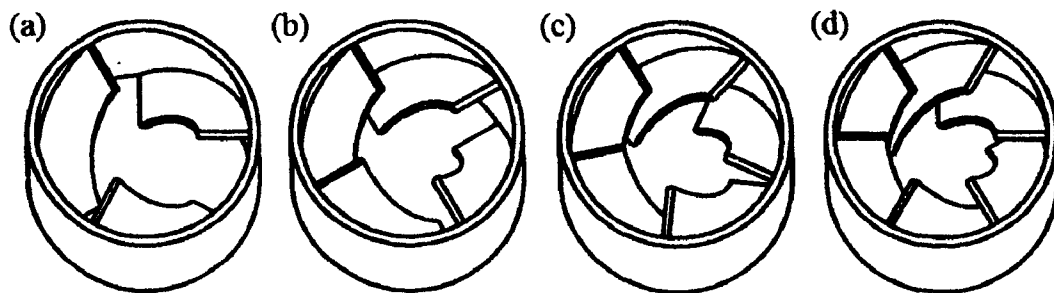


**Figure 6-33:** CAD model of various number of blades ( $N$ ): (a) three blades, (b) four blades, (c) five blades, and (d) six blades.

As expected by the least number of blades from **Eq. 3-5**, the turbine model with three blades shows a significant drop of speed when given the same torque while the other three models showed close results (**Figure 6-34**).

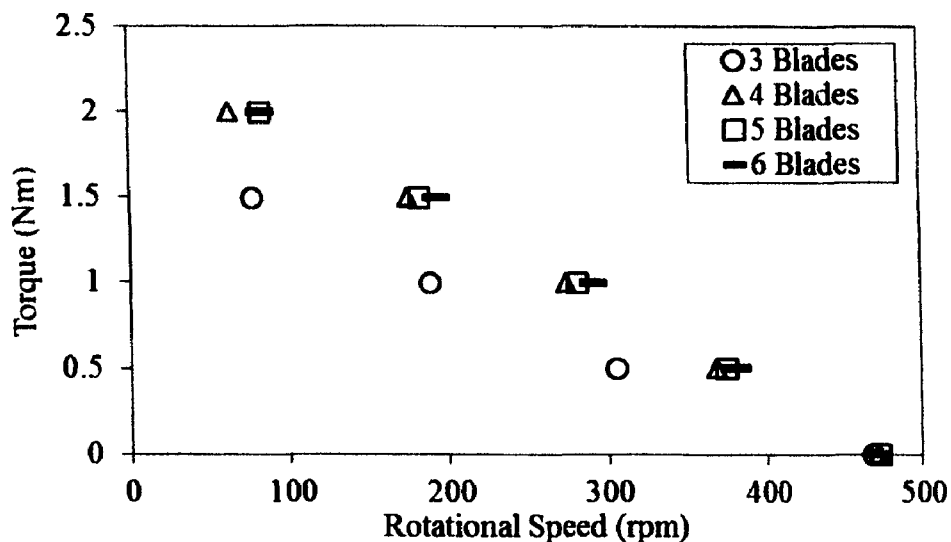


**Figure 6-34:** Numerical torque versus speed as various number of blades ( $N$ ).

Power was estimated using the torque versus speed results (Figure 6-35). As seen from Figure 6-35, there is not much improvement in terms of energy when adding more blades from the original design (four blades). Around 31.88 Watts (242 rpm speed) of maximum power was expected from a six-blade turbine which showing an improvement around 8 % higher than power of a four-blade turbine. However, the maximum power showed a significant decrease around 34 % when we reduced the number of blade from four to three blades.

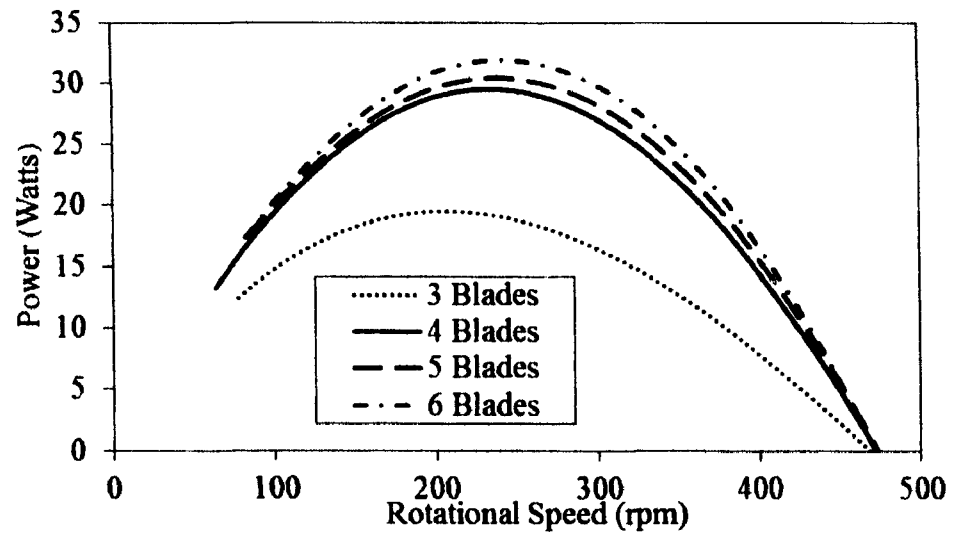


**Figure 6-35:** Power versus speed at various number of blades ( $N$ ).

## **CHAPTER 7**

### **CONCLUSION AND FUTURE WORK**

#### **7.1 Conclusion**

In the dissertation, a custom turbine was developed to extract kinetic energy from the fluid flow within the VDS. The turbine was designed as a module consisting of a rotor and connecting supports such that it could be retrofitted along a drop shaft. The rotor consisted of helical-profile blades that obstructed the near-wall incoming fluid. Fluid energy was transferred via a rotating rotor while subjected with external loads. Research was done in two phases in order to analyze: 1) flow characteristics in the VDS and 2) turbine performance.

In the first phase, numerical models of single-fluid and two-fluid were used to define flow solutions. The single-fluid model treated a problem only in the liquid region and its free surface while the two-fluid model took an account of both the liquid and gases phase. Although the two-fluid model represented more actual behavior of flow in the VDS, it required more computation resources and time to execute. A small-scale VDS (10 cm diameter and 1 m long) was employed for testing in this phase. Numerical solutions were compared with the existing analytical solution and experiments. Results show that both numerical models predicted similar outcome compared with the analytical solutions. In the experiment static pressure was measured along the shaft wall, and it showed a good agreement with analytical and numerical models.

In the second phase, the numerical model of the turbine was implemented with the single fluid model to predict its performance. Analytical solution based on the finite control volume analysis was carried out. Experiments were done to compare numerical solutions and analytical predictions. A large-scale VDS (15 cm diameter and 7.6 m long) was employed for testing in this phase. The experiments were done to evaluate torque and corresponding rotational speed of the turbine which was further used to predict power and efficiency.

Numerical results showed that the turbine did not block the air to flow. This supports that existing VDS could be operated with the turbine without interfering with its original functions.

Two experiments were done to evaluate the turbine's performance. In the first experiment, static torque and highest rotational speed were measured. Results showed that the torque and speed increased proportionally with the flow rate. The experimental results were slightly lower when compared with analytical and numerical solution, but showed similar tendency.

In the second experiment, the dynamic torque was measured. Pulley transmission system with an adjustable magnetic brake was used to provide external loads to the turbine. Torque versus speed curve was obtained by the analytical, numerical, and experimental methods. The results were in good agreement, although the experimental result was slightly lower than the other two.

Parametric study of the turbine's blade was done numerically to improve the turbine performance. Blade configurations including location, angle, width and numbers



were optimized. Results showed that by moving the turbine up closer to the shaft's entrance and increasing the numbers of blade, the highest power was improved.

## **7.2 Future Work**

Several aspects of the turbine developed in this research could be studied further. First, the research could focus on an implementation of an electrical generator. Secondly, as the current research is limited only to a laboratory viewpoint, further investigations of eVortex installed within a real sewer is still required. Lastly, research could focus more on further optimization of the blade's geometry. Although this dissertation numerically improved the turbine, it only optimized the original blade design based on the helical profile. Completely new and better blade configurations could be implemented to provide better functional and practical implementation.

**APPENDIX A**

**AIR FLOW THROUGH VDS**

## AIR FLOW THROUGH VDS

During the process of composing this dissertation, additional study of air flow through the VDS was investigated. The experiment aimed to measure negative static pressure at the inlet structure and air velocity at the center of a vertical drop shaft.

The large scale VDS (Figure 6-8(a)) was used in the experiment and operated with a water flow rate of 190 GPM. The turbine was removed from the VDS; thus, the air through the VDS was only considered. A Pitot tube [67] and a differential pressure transducer [68] with a pressure range up to 800 Pa was used during the experiments to measure air pressure and velocity. Figure A-1 shows photos of the Pitot tube and the pressure transducer.



**Figure A-1:** (a) Pressure transducer with rated maximum of 800 Pa and (b) Pitot tube using in the air measurement.

In the first experiment, the static pressure at the center of the inlet structure was measured along the elevation. A hollow tube connected the pressure transducer were used in this experiment. Figure A-2 shows the air pressure measurement setup. At the end of the tube, there is a custom probe with a small port allowing air to contact with the air inside the tube. The tube was connected to the transducer to read the pressure respective to the atmosphere pressure.

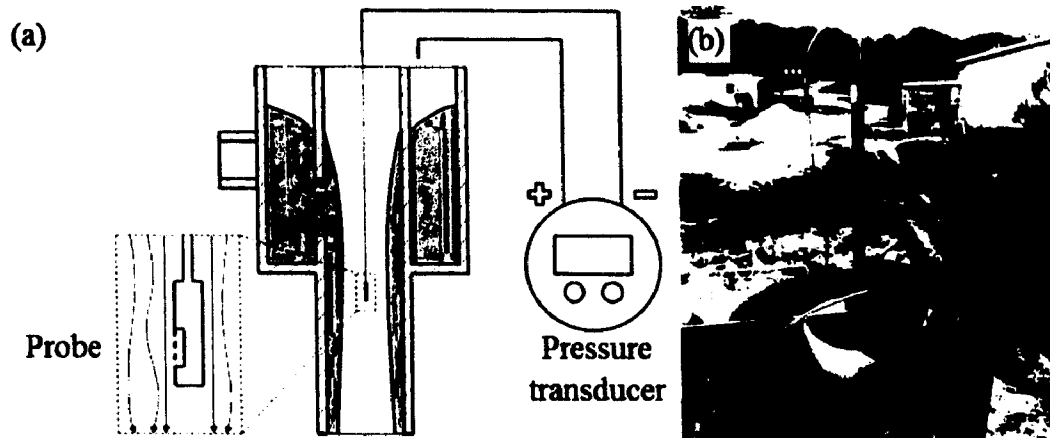


**Figure A-2:** (a) Diagram and (b) actual photo of the air pressure measurement.

In the second experiment, an axial velocity of air at the center and at around 1.2 m (4 ft) below the drop shaft's entrance was measured using a Pitot tube. **Figure A-3** shows the velocity measurement setup. The Pitot tube consists of two ports to measure the total pressure ( $P_t$ ) and the static pressure ( $P_s$ ) as shown in **Figure A-3(a)**. The Pitot tube was inserted to a small hole on the drop shaft's wall. The velocity was calculated using the differential pressure between the total pressure and the static pressure obtained from the Pitot tube. The following equation shows the velocity calculation [47]:

$$V = \sqrt{\frac{2(P_t - P_s)}{\rho}}, \quad \text{Eq. A-1}$$

where  $\rho$  is density of air ( $1.2 \text{ kg/m}^3$ ) at  $25^\circ \text{C}$ . The differential pressure ( $P_t - P_s$ ) was read directly from the pressure transducer.

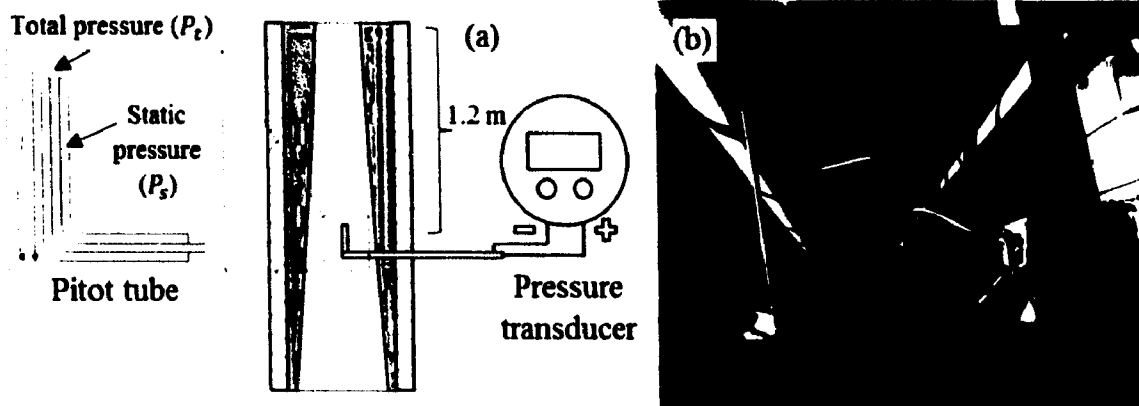


**Figure A-3:** (a) Diagram and (b) actual photo of the velocity measurement.

The experiments were carried out into two cases which the drop shaft's outlet 1) exposed to atmospheric air and 2) submerged inside the water in a pool. **Figure A-4** shows diagram of the outlet in each case. It was expected that the volume of the air flow in the first case was higher than the second because the air would not be blocked by the water from the pool.

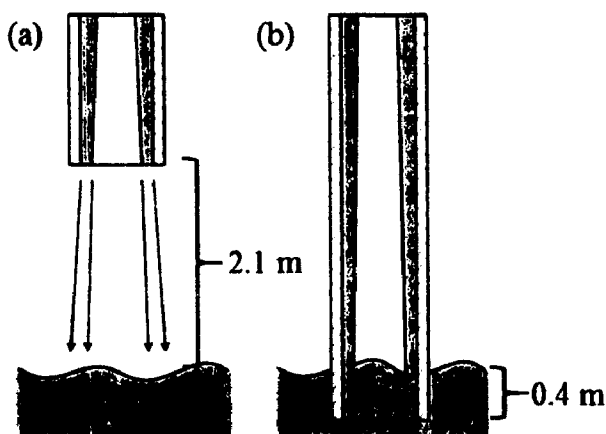


**Figure A-4:** The location of the shaft's outlet when (a) exposed to atmospheric air and (b) submerged in water in a pool.

Numerical modeling of two-fluid flow in the first case (shaft exposed to atmosphere) was done using the Flow3D for comparison.

In the static pressure experiment, air inside the inlet structure of the VDS showed a negative pressure relative to the atmosphere. **Figure A-5** shows the comparison of static pressure from numerical results and experiments. In the first case (shaft exposed to atmosphere), numerical and experimental results show a similar trend where numerical predictions showed lower pressure than the experiment. In the submerged case, the negative pressure could be noticed but less than the first.

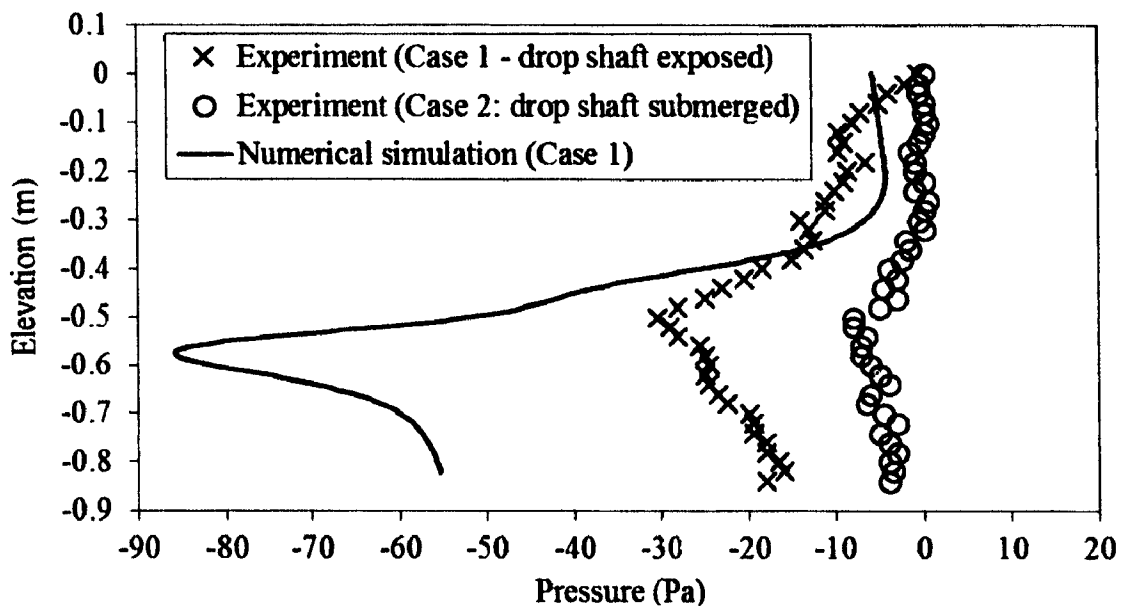


**Figure A-5:** Static pressure of air at the inlet structure.

In the velocity experiment, the data of differential pressure ( $P_t - P_s$ ) from Pitot tube were collected. **Figure A-6** shows the collected data. As seen from **Figure A-6**, the differential pressure from the first case is slightly higher than the second case, but less fluctuated. The average value of the differential pressure was 46.89 Pa from the exposed case and 14.21 Pa from the other case.

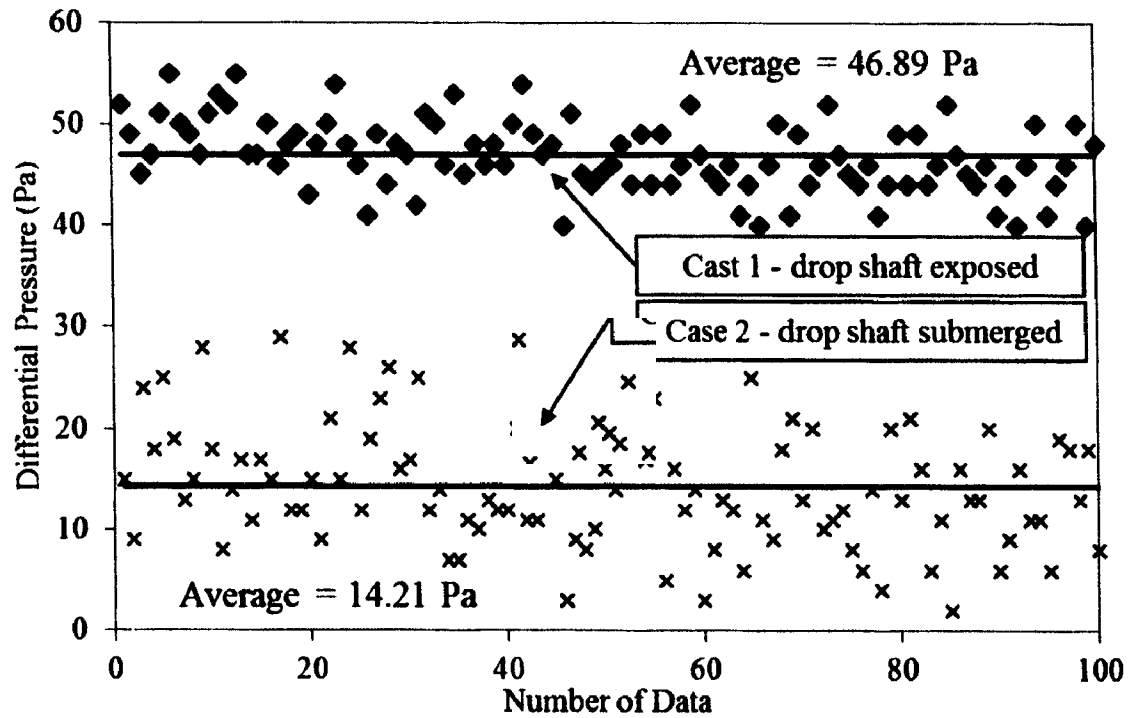


**Figure A-6:** Differential pressure data from Pitot tube.

The axial velocity was calculated using **Eq. A-1** and the results are shown in **Table A-1**. As seen from **Table A-1**, the axial velocity in the exposed case showing similar results from both numerical and experiment. As the air velocity in the submerged case is lower than the first case, the volume of air flowing through the VDS is lesser in this case.

**Table A-1:** Comparison of air flow velocity from the numerical result and experiments.

<b>Flow scenario at shaft outlet</b>	<b>Measured differential pressure (Pa)</b>			<b>Measured air velocity (m/s)</b>			<b>Numerically simulated air velocity (m/s)</b>
	<b>Min</b>	<b>Max</b>	<b>Avg</b>	<b>Min</b>	<b>Max</b>	<b>Avg.</b>	
<b>Case 1: Exposed</b>	40	55	46.89	8.16	9.57	8.84	8.49
<b>Case 2: Submerged</b>	2	29	14.21	3.33	6.95	4.86	N/A



**APPENDIX B**

**EXAMPLE OF ANALYTICAL SOLUTION**

### EXAMPLE OF ANALYTICAL SOLUTION

In Appendix B, an example problem of the turbine's performance is solved using the analytical method. The calculation begins with identifying flow characteristics using the existing analytical solution of flow in the VDS (mentioned in Chapter 2) and uses the flow solutions to determine the turbine's performances (mentioned in Chapter 4).

In this calculation, water of 190 GPM ( $Q = 0.011987 \text{ m}^3/\text{s}$ ) flowing through the VDS with 6-inche diameter ( $D = 0.1524 \text{ m}$ ) is shown. Turbine was installed at 5.639 m (18.5 ft) below the entrance. The geometry of the turbine is given in **Table 3-1**.

As the analytical solution requires initial flow characteristics at the entrance, the characteristics were obtained from the numerical methods and the average velocity components are shown in **Table B-1**

**Table B-1:** Numerical result of average velocity at the shaft entrance.

Velocity components	Average values (m/s)
Axial ( $V_{z_0}$ )	1.516571
Tangential ( $V_{t_0}$ )	1.332089

Knowing the average axial velocity ( $V_{z_0}$ ), flow rate ( $Q$ ) and shaft diameter ( $D$ ), relative thickness ( $t_0$ ) could be found using **Eq. 2-13**:

$$V_{z_0} = \frac{4Q}{\pi D^2 t_0 (2 - t_0)}, \quad \text{Eq. B-1}$$

$$t_0 = 0.247205. \quad \text{Eq. B-2}$$

Knowing the average tangential velocity ( $V_{t_0}$ ), relative thickness ( $t_0$ ) and shaft diameter ( $D$ ), the circulation ( $\Omega_0$ ) could be found using Eq. 2-12:

$$V_{t_0} = \frac{4\Omega_0}{(2 - t_0)D}, \quad \text{Eq. B-3}$$

$$\Omega_0 = 0.088959 \text{ m}^2/\text{s}. \quad \text{Eq. B-4}$$

The average velocity ( $V_0$ ) magnitude and its angle ( $\theta_0$ ) could also be found as follows:

$$V_0 = \sqrt{V_{z_0}^2 + V_{t_0}^2} = 2.018526 \text{ m/s}, \quad \text{Eq. B-5}$$

$$\theta_0 = \tan^{-1} \frac{V_{z_0}}{V_{t_0}} = 0.849787 \text{ rad}. \quad \text{Eq. B-6}$$

After knowing the initial flow conditions, flow characteristics along the drop shaft are estimated from Eq. 2-8 and Eq. 2-9 using Euler's method [69]. These two equations are rewritten as the following, respectively:

$$\Omega_{n+1} = \Omega_n - \Delta z \frac{f\pi D^2}{16Q} V_n V_{t_n}, \quad \text{Eq. B-7}$$

$$V_{z_{n+1}} = V_{z_n} + \Delta z \left[ \frac{g}{V_{z_n}} - \frac{f\pi D V_n V_{z_n} (1 - M)}{8Q} \right] / (1 - T), \quad \text{Eq. B-8}$$

where

$$M = \frac{1}{2t_n \tan^2 \theta_n} \left[ \frac{1}{(1 - t_n)^2} + 2 \ln(1 - t_n) - 1 \right], \quad \text{Eq. B-9}$$

$$T = \frac{t_n (2 - t_n)^3}{8 \tan^2 \theta_n (1 - t_n)^4}, \quad \text{Eq. B-10}$$

$$n = 0, 1, 2, 3, 4, \dots \quad \text{Eq. B-11}$$

An increment of length ( $\Delta z$ ) should be small enough to provide more accurate solutions, and in this problem, it is given as  $\Delta z = 0.0001$  m. The elevation below the shaft's entrance could be expressed as:

$$z_{n+1} = z_n + \Delta z. \quad \text{Eq. B-12}$$

In this problem,  $z_0 = 0$  m refers to the elevation at the shaft's entrance while  $z_{5639} = 5.639$  m ( $n = 5639$ ) is where the turbine was installed. Therefore, the initial flow characteristics at the entrance is subscripted with  $n = 0$ . The first iteration ( $n = 0$ ) of the above equations are solved as the following:

$$\Omega_1 = \Omega_0 - \Delta z \frac{f\pi D^2}{16Q} V_0 V_{t_0}, \quad \text{Eq. B-13}$$

$$\Omega_1 = 0.088938 \text{ m}^2/\text{s}, \quad \text{Eq. B-14}$$

$$M = \frac{1}{2t_0 \tan^2 \theta_0} \left[ \frac{1}{(1-t_0)^2} + 2 \ln(1-t_0) - 1 \right], \quad \text{Eq. B-15}$$

$$M = 0.307254, \quad \text{Eq. B-16}$$

$$T = \frac{t_0(2-t_0)^3}{8 \tan^2 \theta_0 (1-t_0)^4}, \quad \text{Eq. B-17}$$

$$T = 0.400207, \quad \text{Eq. B-18}$$

$$V_{z_1} = V_{z_0} + \Delta z \left[ \frac{g}{V_{z_0}} - \frac{f\pi D V_0 V_{z_0}}{8Q} \right] / (1-T), \quad \text{Eq. B-19}$$

$$V_{z_1} = 1.526956 \text{ m/s}. \quad \text{Eq. B-20}$$

$f$  is a friction factor which was given as 0.02. Knowing  $V_{z_1}$  and  $\Omega_1$ , the new  $t_1$  and  $V_{t_1}$  could be solved using Eq. 2-13 and Eq. 2-12. Further,  $V_1$  and  $\theta_1$  could be found out by using calculations mentioned earlier.

At the end of the first iteration ( $n = 0$ ), other characteristic parameters are calculated as the following:

$$t_1 = 0.245250, \quad \text{Eq. B-21}$$

$$V_{t_1} = 1.330300 \text{ m/s}, \quad \text{Eq. B-22}$$

$$V_1 = 2.025165 \text{ m/s}, \quad \text{Eq. B-23}$$

$$\theta_1 = 0.854117 \text{ rad.} \quad \text{Eq. B-24}$$

Repeat the same steps mentioned earlier for further iterations until it reaches the 5639<sup>th</sup> iteration ( $n = 5638$ ) where  $z_{5638} = 5.639$  m. At this iteration, axial velocity ( $V_{z_{5639}}$ ), circulation ( $\Omega_{5639}$ ) and relative thickness ( $t_{5639}$ ) are found as:

$$V_{z_{5639}} = 4.612395 \text{ m/s}, \quad \text{Eq. B-25}$$

$$\Omega_{5639} = 0.007078 \text{ m/s}, \quad \text{Eq. B-26}$$

$$t_{5639} = 0.073971. \quad \text{Eq. B-27}$$

Power available ( $P_a$ ) at this location is calculated using Eq. 6-4. The result is:

$$P_a = \rho Q \left[ \frac{V_{z_{5639}}^2}{2} + \frac{2\Omega_{5639}^2}{D^2(1-t_{5639})^2} \right], \quad \text{Eq. B-28}$$

$$P_a = 127.567 \text{ Watts.} \quad \text{Eq. B-29}$$

The axial velocity and circulation are used to calculate torque ( $\tau$ ) versus rotational speed ( $\omega$ ) of the turbine using Eq. 4-22:

$$\tau = -\rho Q \sqrt{(RV_{z_{5639}})^2 + (\Omega_{5639} - \omega R^2)^2} \cos(\beta - \alpha) \sin \alpha, \quad \text{Eq. B-30}$$

where

$$\beta = \tan^{-1} \frac{\Omega_{5639} - \omega R^2}{RV_{z_{5639}}}. \quad \text{Eq. B-31}$$

With the blade angle  $\alpha = 45^\circ$  ( $\pi/4$  rad), the torque versus speed is found as the following:

$$\tau = -8.476089 \cdot \sqrt{0.123527 + (0.007078 - \omega \cdot 0.0762^2)^2} \cdot \cos\left(\beta - \frac{\pi}{4}\right), \quad \text{Eq. B-32}$$

where

$$\beta = \tan^{-1} \frac{0.007078 - \omega \cdot 0.0762^2}{0.351464}. \quad \text{Eq. B-33}$$

By substituting  $\tau = 0$  Nm and  $\omega = 0$  rad/s, the maximum speed ( $\omega = 61.75$  rad/s) and the maximum torque ( $\tau = -2.15$  Nm) could be solved, respectively. The negative sign of the torque refers that it occurs opposite the rotating direction. The power and efficiency could be found using Eq. 4-24 and Eq. 6-3.

## BIBLIOGRAPHY

- [1] U.S. Energy Information Administration, "Monthly Energy Review November 2014," Washington, DC, 2014.
- [2] U.S. Environmental Protection Agency, "Inventory of U.S. Greenhouse Gas Emissions and Sinks 1990-2013," Washington, DC, 2015.
- [3] U.S. Energy Information Administration, "Lower electricity-related CO<sub>2</sub> emissions reflect lower carbon intensity and electricity use," 23 October 2014. [Online]. Available: <http://www.eia.gov/todayinenergy/detail.cfm?id=18511>. [Accessed 11 July 2015].
- [4] U.S. Energy Information Administration, "Annual Energy Outlook 2014 with Projection to 2040," Washington, DC, 2014.
- [5] S. William, Drop Structure Design for Waste water and Stormwater Collection Systems, Parsons Brinckerhoff Quade & Douglas, Inc., 2001.
- [6] The City of Columbus, "OARS Deep Sewer Tunnel," [Online]. Available: <http://www.columbus.gov/Templates/Detail.aspx?id=38013#>. [Accessed 11 July 2015].
- [7] N. Rajaratnam, A. Mainali and C. Hsung, "Observation of flow in vertical dropshafts in urban drainage system," *Journal of Environmental Engineering*, vol. 123, no. 5, pp. 486-497, 1997.
- [8] F. Banister, W. Moeller Jr, E. Natarius and K. Sampson, "Spin away odor and decay in sewage drop structures," *Water Engineering and Management*, vol. 146, no. 2, pp. 13-18, 1999.
- [9] IPEX Inc., "Vortex Flow: Insert for sewer odor and corrosion control," [Online]. Available: <http://www.ipexamerica.com/Content/Products/Product.aspx?IsDownload=true&FileId=5130&ProductId=57>. [Accessed 11 July 2015].
- [10] D. Vischer and W. Hager, "Vortex drops," in *Energy Dissipators: IAHR Hydraulic Structure Design manual 9*, CRC Press, 1995, pp. 167-181.
- [11] Water Environment Research Foundation, "Wastewater Sludge: A New Resource for Alternative Energy," Alexandria, VA, 2008.

- [12] I. Shizas and D. Bagley, "Experimental determination of energy content of unknown organics in municipal wastewater streams," *Journal of Energy Engineering*, vol. 130, no. 2, pp. 45-53, 2004.
- [13] Water Environment Research Foundation, "Energy Production and Efficiency Research: The Roadmap to Net-Zero Energy," Alexandria, VA, 2011.
- [14] The National Association of Clean Water Agencies, "Renewable Energy Recovery Opportunities from Domestic Wastewater," Washington, DC, 2009.
- [15] G. Tchobanoglous and F. Burton, "Wastewater Characteristics," in **WASTEWATER ENGINEERING Treatment, Disposal, and Reuse Third Edition**, McGraw-Hill, Inc., 1991.
- [16] N. Cheremisinoff, "Treating the Sludge," in *Handbook of Water and Wastewater Treatment Technologies*, Butterworth-Heinemann, 2002.
- [17] U.S. Environmental Protection Agency, "Biomass Combined Heat and Power Catalog of Technologies," Washington, DC, 2007.
- [18] E. Ryckebosch, M. Drouillon and H. Vervaeren, "Techniques for transformation of biogas to biomethane," *Biomass and Bioenergy*, vol. 35, no. 5, pp. 1633-1645, 2011.
- [19] National Biosolids Partnership, "Manual of Good Practice for Biosolids," Water Environment Federation, Alexandria, VA, 2011.
- [20] U.S. Environmental Protection Agency, "Use of Incineration for Biosolids Management," Washington, DC, 2003.
- [21] N. Nipattummakul, A. Ahmed, S. Kerdsuman and A. Gupta, "High temperature steam gasification of wastewater sludge," *Applied Energy*, vol. 87, no. 12, pp. 3729-3734, 2010.
- [22] A. Bridgwater, D. Meier and D. Radlein, "An overview of fast pyrolysis of biomass," *Organic Geochemistry*, vol. 30, no. 12, pp. 1479-1493, 1998.
- [23] B. Logan, B. Hamelers, R. Rozendal, U. Schröder, J. Keller, S. Freguia, P. Aelterman, W. Verstraete and K. Rabaey, "Microbial fuel cells: Methodology and technology," *Environmental Science and Technology*, vol. 40, no. 17, pp. 5181-5192, 2006.
- [24] L. Brennan and D. Owen, "Biofuels from microalgae-A review of technologies for production, processing and extractions of biofuel and co-products," *Renewable and Sustainable Energy Reviews*, vol. 14, no. 2, pp. 557-577, 2010.



- [25] L. Wong, K. Mui and Y. Guan, "Shower water heat recovery in high-rise residential buildings of Hong Kong," *Applied Energy*, vol. 87, no. 2, pp. 703-709, 2010.
- [26] N. Baek, U. Shin and J. Yoon, "A study on the design and analysis of heat pump heating system using wastewater as a heat source," *Solar Energy*, vol. 78, no. 3, pp. 427-440, 2005.
- [27] Industrial Technologies Program, "Waste Heat Recovery: Technology and Opportunities in U.S. Industry," U.S. Department of Energy, Washington, DC, 2008.
- [28] U.S. Environmental Protection Agency, "Renewable Energy Fact Sheet: Low-Head Hydropower from Wastewater," Washington, DC, 2013.
- [29] G. Crawford and J. Sandio, "Energy Efficiency in Wastewater Treatment in North America: A Compendium of Best Practices and Case Studies of Novel Approaches," Water Environment Research Foundation, Alexandria, VA, 2010.
- [30] R. Schultz, Low Head Powers Wastewater Plant, Arlins Height, IL: *Roads & Bridges*, 2000.
- [31] Massachusetts Water Resources Authority, "Renewable and Sustainable Energy Initiatives at Deer Island," July 2013. [Online]. Available: <http://www.mwra.com/03sewer/html/renewableenergydi.htm>. [Accessed 11 July 2015].
- [32] R. David, "Sewer line power generating system". U.S. Patent 7429803 B2, 2008.
- [33] L. Energy, "LucidPipe," 2011. [Online]. Available: <http://www.lucidenergy.com/lucid-pipe/>. [Accessed 11 July 2015].
- [34] D. Farb, "Benkatina hydroelectric turbine". U.S. Patent 20090160193 A1, 2009.
- [35] M. Kellenberger, "Wirbelfallschächte in der kanalisationstechnik," VAW-Mitteilung 98, ETH, Zurich, Switzerland, 1988.
- [36] S. Jain and J. Kennerdy, "Vortex-flow drop structure for the Milwaukee Metropolitan Sewerage District Inline Storage System, IHR Report No. 264," Iowa Institute of Hydraulic Research, The University of Iowa, Iowa, IA, 1983.
- [37] W. Hager, "Head-discharge relation for vortex shaft," *Journal of Hydraulic Engineering*, vol. 111, no. 6, pp. 1015-1020, 1985.
- [38] W. Hager, "Vortex drop inlet for supercritical approaching flow," *Journal of Hydraulic Engineering*, vol. 116, no. 8, pp. 1048-1054, 1990.

- [39] M. Quick, "Analysis of spiral vortex and vertical slot vortex drop shafts," *Journal of Hydraulic Engineering*, vol. 116, no. 3, pp. 309-325, 1990.
- [40] S. Jain, "Tangential vortex-inlet," *Journal of Hydraulic Engineering*, vol. 110, no. 12, pp. 1693-1699, 1984.
- [41] D. Yu and J. Lee, "Hydraulics of tangential vortex intake for urban drainage," *Journal of Hydraulic Engineering*, vol. 135, no. 3, pp. 164-174, 2009.
- [42] G. Del Giudice, C. Gisonni and G. Rasulo, "Design of scroll vortex inlet for supercritical approach flow," *Journal of Hydraulic Engineering*, vol. 163, no. 10, pp. 837-841, 2010.
- [43] S. Jain, "Free-surface swirling flow in vertical drop shaft," *Journal of Hydraulic Engineering*, vol. 113, no. 10, pp. 1278-1289, 1987.
- [44] C. Zhao, D. Zhu and Z. Liu, "Experimental study of flow in a vortex drop shaft," *Journal of Hydraulic Engineering*, vol. 132, no. 1, pp. 61-68, 2006.
- [45] H. Chen, W. Xu, J. Deng, Z. Niu, S. Liu and W. Wang, "Theoretical and experimental studies of hydraulic characteristics of discharge tunnel with vortex drop," *Journal of Hydrodynamics*, vol. 22, no. 4, pp. 582-589, 2010.
- [46] M. Quick, "The annular hydraulic jump," *Civil Engineering and Public Works Reviews*, vol. 56, no. 662, pp. 1176-1179, 1961.
- [47] B. Munson, D. Young and T. Okiishi, *Fundamentals of Fluid Mechanics Fifth Edition*, John Wiley & Sons, Inc., 2006.
- [48] W. Peng, *Fundamental of Turbomachinery*, John Wiley & Sons, Inc., 2008.
- [49] R. Jia, S. Zhang and L. Hu, "Numerical simulation of Hydraulic Characteristics in Tangential Vortex Dropshaft," *Advanced Material Research*, Vols. 594-597, pp. 2066-2069, 2012.
- [50] K. Nielsen and A. Davis, "CFD Analysis of Vortex Dropshaft Structure," *World Environmental and Water Resources Congress*, pp. 1-8, 2008.
- [51] V. Sousa, F. Bombardelli and H. Chanson, "Numerical simulation of rectangular dropshafts using a volume-of-fluid (VoF) technique," in *33rd IAHR Biennial Congress, IAHR-ASCE-EWRI*, Vancouver, Canada, 2009.
- [52] Flow Science, Inc., "FLOW#D v. 9.4 user's manual," Santa Fe, NM, 2010.
- [53] V. Yakhot and S. Orszag, "Renormalization Group Analysis of Turbulence," *Journal of Scientific Computing*, vol. 1, no. 1, 1986.

- [54] Q. Hou and Z. Zou, "Comparison between Standard and Renormalization Group  $k-\epsilon$  Models in Numerical Simulation of Swirling Flow Tundish," *ISIJ International*, vol. 45, no. 3, pp. 325-330, 2005.
- [55] C. Hirt and B. Nichols, "Volume of Fluid (VOF) method for dynamics of free boundaries," *Journal of Computational Physics*, vol. 39, pp. 201-225, 1981.
- [56] G. F. Yao, "Development of New Pressure-Velocity Solvers in Flow-3D," FSI-04-TN68, Flow Science, Inc., Santa Fe, NM, 2004.
- [57] OpenCFD. Ltd., "OpenFOAm, The Open-Source CFD Tool Box, User Guide v 1.7.1," Berkshire, UK, 2010.
- [58] H. Rusche, "Computational fluid dynamics of disper two-phase flow at high phase fractions, Doctoral thesis," University of London, 2002.
- [59] G. Wei, "A fixed-meshed method for general moving objects in fluid flow," *Modern Physics Letters B*, vol. 19, no. 28-29, pp. 1719-1722, 2005.
- [60] "Pressure sensors P51-3-G-UB-I36-5V," SSI Technologies Inc., [Online]. Available: <http://www.digikey.com/product-search/en?mpart=P51-3-G-UB-I36-5V-000-000&vendor=734>. [Accessed 11 July 2015].
- [61] "Paddlewheel Flow Sensors Series FP-5300, User's Guide," Omega, [Online]. Available: <http://www.omega.com/Manuals/manualpdf/M3814.pdf>. [Accessed 11 July 2015].
- [62] "Miniature Low-Profile Tension Links LC703-10, User's Guide," Omega, [Online]. Available: <http://www.omega.com/pressure/pdf/LC703.pdf>. [Accessed 11 July 2015].
- [63] "Neiko Digital Laser Photo Tachometer 20713A," Neiko Tools USA, [Online]. Available: <http://www.toolplanet.com/product/Neiko-Digital-Laser-Photo-Tachometer>. [Accessed 11 July 2015].
- [64] "Magnetic Particle Brake B15," Placid Industries Inc., [Online]. Available: <http://www.placidindustries.com/spec.b15.pdf>. [Accessed 11 July 2015].
- [65] ONSITE SYCOM Energy Corporation, "Review of combined heat and power technologies," U.S. Department of Energy, Washington, DC, 1999.
- [66] "Estimating the frictional moment," SKF Group, [Online]. Available: <http://www.skf.com/group/products/bearings-units-housings/ball-bearings/principles/friction/estimating-frictional-moment/index.html>. [Accessed 11 July 2015].

- [67] "Model 116T Telescoping Pitot tube," Dwyer Instrumentals Inc., [Online]. Available: [http://www.dwyer-inst.com/PDF\\_files/166T\\_IOM.pdf](http://www.dwyer-inst.com/PDF_files/166T_IOM.pdf). [Accessed 11 July 2015].
- [68] "Series DM-2000 Differential Pressure Transmitter," Dwyer Instrumentals Inc., [Online]. Available: [http://www.dwyer-inst.com/PDF\\_files/E\\_43\\_DM.pdf](http://www.dwyer-inst.com/PDF_files/E_43_DM.pdf). [Accessed 11 July 2015].
- [69] S. Chapra and R. Canale, Numerical Methods for Engineers Sixth Edition, McGraw-Hill, 2010.
- [70] Office of Energy Efficiency and Renewable Energy, "Types of hydropower plants," U.S. Department of Energy, [Online]. Available: <http://energy.gov/eere/water/types-hydropower-plants#sizes>. [Accessed 11 July 2015].